

Contents

1	Neutral MSSM Higgs Bosons Search...	3
1.1	Introduction	5
1.1.1	The Higgs Sector in the MSSM	5
1.1.2	Signal and Background Processes	7
1.1.3	Analysis Strategy	9
1.1.4	Data and Simulated Event Samples	12
1.2	Event Selection and Categorization	13
1.2.1	The Common Selection Criteria	13
1.2.2	b-vetoed Event Category	14
1.2.3	b-tagged Event Category	17
1.2.4	Mass Reconstruction with MMC Technique	17
1.3	Background Prediction and Validation	21
1.3.1	Validation of the $t\bar{t}$ Background Prediction	21
1.3.2	Multi-jet Background Measurement	24
1.3.3	$Z \rightarrow \tau\tau + \text{Jets}$ Background Measurement	30
1.4	Systematic Uncertainties	34
1.4.1	Detector-related Systematics Uncertainties	34
1.4.2	Theoretical Uncertainties	37
1.4.3	Systematic Uncertainties of the $Z/\gamma^* \rightarrow \tau\tau$ Embedded Sample	40
1.4.4	QCD Multi-Jet Systematic Uncertainties	42
1.5	Results	44
1.5.1	Statistical Procedure	44
1.5.2	Exclusion Limits on the Signal Production	48

A	QCD Trigger bias	71
B	QCD Additional Plots	73
C	Limits cross checks and additional plots	75
C.1	The ABCD Method	75
C.2	Additional Limit Checks	76
C.3	Shape Systematics	89

Chapter 1

Search for neutral MSSM

Higgs Bosons in

$A/h/H \rightarrow \tau^+\tau^- \rightarrow e\mu + 4\nu$ decays

In light of the recent discovery of a Higgs boson with mass of ~ 126 GeV at the LHC [16,17], it remains an open question whether this new particle is the only missing piece of the electroweak symmetry breaking sector or whether it is one of several Higgs bosons predicted in theories that go beyond the SM. The most recent measurements [125–128] of its properties shows this new boson to be, within experimental uncertainties, fully compatible with the SM Higgs boson. Nevertheless, such a new particle can also still be accommodated within several theories beyond the standard model (BSM). Among all of them, Supersymmetry is a theoretically favoured scenario as the most predictive framework beyond the Standard Model.

This chapter presents the search for the neutral MSSM Higgs bosons decaying into pairs of tau leptons in the fully leptonic final state, published in Ref. [1] as a part of the search for the neutral MSSM Higgs bosons in all final states of the tau leptons decay. The search is based on 20.3 fb^{-1} of data at a centre-of-mass energy of $\sqrt{s} = 8 \text{ TeV}$ recorded by the ATLAS experiment during 2012. This chapter is organised as follows: a brief summary of the

¹to Sandra: I'll remove this sentence if Conf note wont be ready in time

MSSM Higgs sector and an introduction to the analysis strategy is given in Section 1.1, while the event selection and categorization are described in Section 1.2. Section 1.3 describes the estimation of the backgrounds and in Section 1.4 methods to evaluate systematic uncertainties are discussed. Finally, in section 1.5, an overview of the statistical methods employed along with the corresponding result of the search are presented.

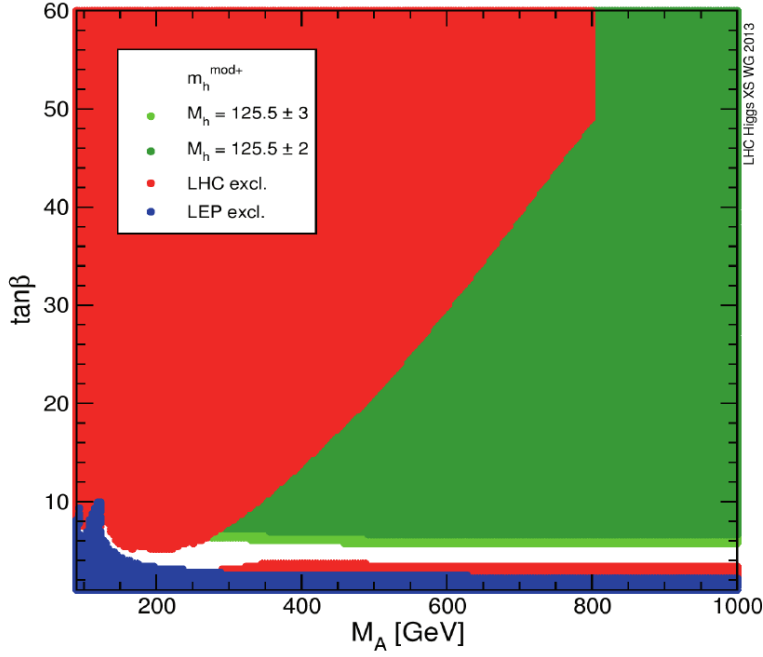


Figure 1.1: Excluded and allowed regions of the $m_A - \tan\beta$ parameter space for the m_h^{mod+} MSSM benchmark scenario. Excluded regions are determined based on direct Higgs boson searches at LEP (blue) and LHC (red). The two green bands correspond to the parameter regions which are compatible with the assumption that the lightest MSSM Higgs boson, h , has a mass respectively of $M_h = 125.5 \pm 2$ (dark green) or 125.5 ± 3 GeV (light green). For more detail see [4].

1.1 Introduction

1.1.1 The Higgs Sector in the MSSM

In the Minimal Supersymmetric extension of the Standard Model (MSSM) [36,37] the Higgs sector is composed of two Higgs doublets of opposite hyper-charge, resulting in five observable Higgs bosons: two of these are neutral and CP -even (h, H), one is neutral and CP -odd (A) and two are charged (H^\pm). At tree level their properties such as masses, widths and branching ratios can be predicted in terms of only two parameters, often chosen to be the mass of the CP -odd Higgs boson

m_A and the ratio of the vacuum expectation values of the two Higgs doublets $\tan \beta$ (for more details see chapter ??). The MSSM predicts the existence of a Higgs boson with properties that resemble those of a SM Higgs boson in large regions of its parameter space. This is usually the case for the lightest Higgs boson, h , while the other two, H and A , tend to be degenerate in mass and decouple from gauge bosons. On the other hand, the couplings of the latter two Higgs bosons with down (up) type fermions are enhanced (suppressed) proportionally to the value of $\tan \beta$, meaning that for large $\tan \beta$ bottom-quark and τ lepton will play an important role for the Higgs bosons production and its decays.

The two most relevant MSSM Higgs bosons production mechanisms at the LHC are gluon fusion, $gg \rightarrow A/H/h$, and the production in association with b -quarks, $pp \rightarrow b(b)A/h/H$, the latter becoming increasingly important for large values of $\tan \beta$. These two are the only production mechanisms considered in this analysis. Assuming there are no decays into supersymmetric particles since these are too heavy, the favoured neutral MSSM Higgs bosons decay mode is the decay into a pair of b -quark and anti-quark, $A/h/H \rightarrow b\bar{b}$. This is followed, for the CP-odd A and CP-even H Higgs bosons, by the decay into pairs of τ leptons. Given that it is very difficult to distinguish the former decay from the large $b\bar{b}$ background, the decay mode $A/h/H \rightarrow \tau^+\tau^-$ provides the highest sensitivity in the search for neutral MSSM Higgs bosons.

Searches for neutral MSSM Higgs bosons have been performed at LEP [64], the Tevatron [65] and the LHC [66,67]. In the following the search for the neutral MSSM Higgs bosons in the final state $A/h/H \rightarrow \tau^+\tau^- \rightarrow e\mu + 4\nu$ is presented. This search is complementary to the searches in other $\tau^+\tau^-$ final states characterised by the presence of one or two hadronically decaying τ leptons. Despite of the fact that the $\tau\tau$ branching ration in $e\mu + 4\nu$ is only 6%, this decay channel provides a sensitivity to the signal comparable to those in other $\tau\tau$ final states, especially for low m_A values. This is mainly due to the high transverse momentum threshold at the trigger level for hadronically decaying τ leptons.

As it is impractical for an experimental search to explore the full parameter space of the MSSM, which has many free parameters, several benchmark scenarios

are introduced by fixing all except m_A and $\tan\beta$ parameters to values typical for most interesting physics cases. With the recent Higgs boson discovery, benchmark scenarios of the MSSM have been updated to accommodate for new experimental constraints. As an example, Figure 1.1 shows the currently excluded and allowed regions of the MSSM parameter space for the m_h^{mod+} updated benchmark scenario. In this scenario a large region of the $m_A - \tan\beta$ parameter space is compatible with the assumption that the observed Higgs boson correspond to the supersymmetric CP-even neutral Higgs boson, h . A large part of this parameter space is still experimentally unexplored, this is a strong motivation to pursue the search for additional neutral MSSM Higgs bosons.

1.1.2 Signal and Background Processes

Signal events in which the neutral MSSM Higgs bosons decay through $A/h/H \rightarrow \tau^+\tau^- \rightarrow e\mu + 4\nu$ process are characterised by the presence of one electron and one muon of opposite charge. These two leptons are isolated and have relatively high transverse momenta. In addition, four neutrinos contribute to the missing transverse energy in the event. Figure 1.2 shows leading order Feynman diagram for the two considered signal production modes, gluon fusion and in association with b -quarks. The presence (absence) of a b -jet in the final state serves as a main characteristic for the event categorization in the latter (former) case, as described later on.

The described signal topology is common to several other known SM background processes which in general have higher cross sections than the sought signal. The dominant background processes are the $Z/\gamma^* \rightarrow \tau^+\tau^-$ production either via Drell-Yan process or in association with jets and the top quark production ($t\bar{t}$ and single top quark production). Additional significant background contributions originate from the dibosons production (WW, WZ, ZZ) and QCD multi-jet events with non-prompt leptons from hadron decay. Vector boson production ($W \rightarrow \ell\nu$ or $Z \rightarrow \ell\ell$, where $\ell \equiv e, \mu$) in association with jets is also considered, but has small impact on the total background contamination. Examples of leading order Feynman diagrams for the dominant background processes are shown in

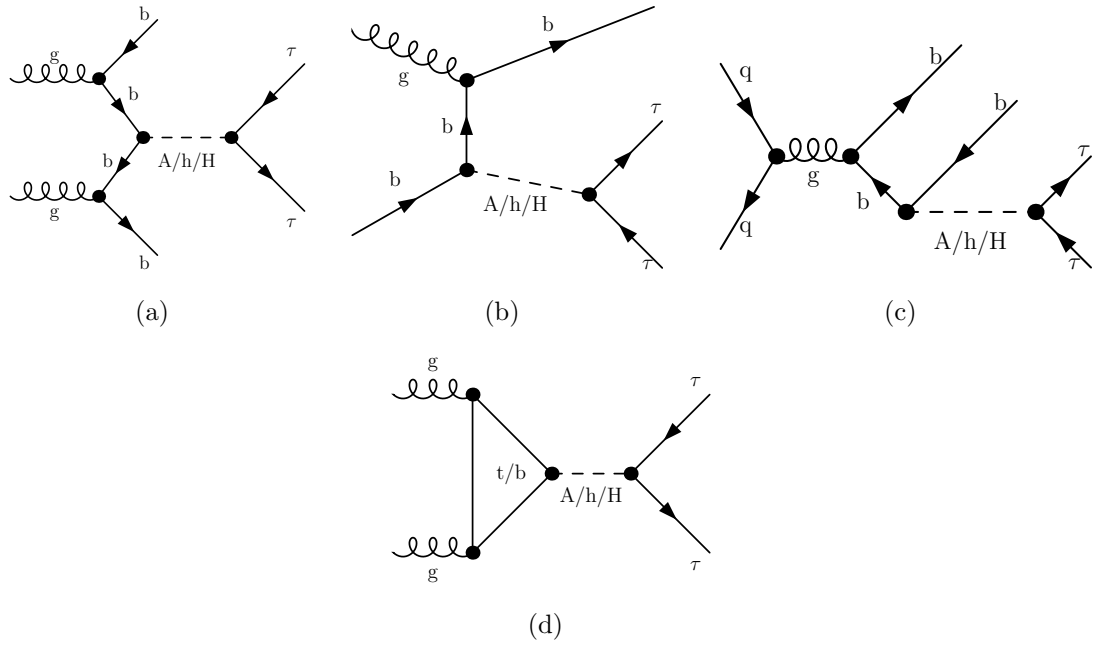


Figure 1.2: Feynman diagram for the production of the neutral MSSM Higgs bosons in association with b -quarks (a,b,c) and via gluon fusion (d) process, subsequent decay in tau lepton pairs is considered.

Process	Cross-section (pb) [\times BR]
Signal ($m_A = 150$ GeV, $\tan \beta = 20$, m_h^{mod} scenario)	
$gg \rightarrow A/h/H \rightarrow \tau\tau \rightarrow e\mu + 4\nu$	0.24/0.20/0.95
$pp \rightarrow b\bar{b}A/h/H \rightarrow \tau\tau \rightarrow e\mu + 4\nu$	0.53/0.05/0.49
Backgrounds	
$W \rightarrow \ell\nu + \text{jets}$	12.22×10^3
$Z/\gamma^* \rightarrow \ell\ell + \text{jets}$	5.5×10^3
$t\bar{t} \rightarrow \ell\ell + X$	137.3
Single top quark (t -, s - and Wt -channels) $\rightarrow \ell + X$	28.4, 1.8, 22.4
Dibosons (WW, WZ and ZZ) $\rightarrow \ell\ell + X$	20.6, 6.8, 1.55

Table 1.1: The cross sections multiplied by the relevant branching ratios (BR) for signal and the considered background processes. The symbol ℓ stands for $\ell = (e, \mu, \tau)$. Signal cross sections are calculated for the m_h^{mod} scenario assuming $m_A = 150$ GeV and $\tan \beta = 20$. The masses of the other two neutral MSSM Higgs bosons are in this case $m_H = 151$ GeV and $m_h = 125$ GeV.

Figure 1.3. The production cross sections times the relevant branching fraction for signal and background processes are summarized in Table 1.1.

1.1.3 Analysis Strategy

In this thesis a search for the MSSM $A/h/H \rightarrow \tau^+\tau^- \rightarrow e\mu + 4\nu$ decays is presented. The $ee + 4\nu$ and $\mu\mu + 4\nu$ final states are not considered since a large background contribution is expected from $Z \rightarrow ee$ and $Z \rightarrow \mu\mu$ decays, respectively, such that the sensitivity of the search in these final state is significantly reduced.

Candidate events are selected based on the topological properties of the Higgs boson production and decay. The presence of exactly one electron and one muon is required in each event. Electron and muon are required to be isolated and of opposite electrical charge. The events are categorized into two mutually orthogonal event categories. In the so called *b-vetoed* event category, the absence of

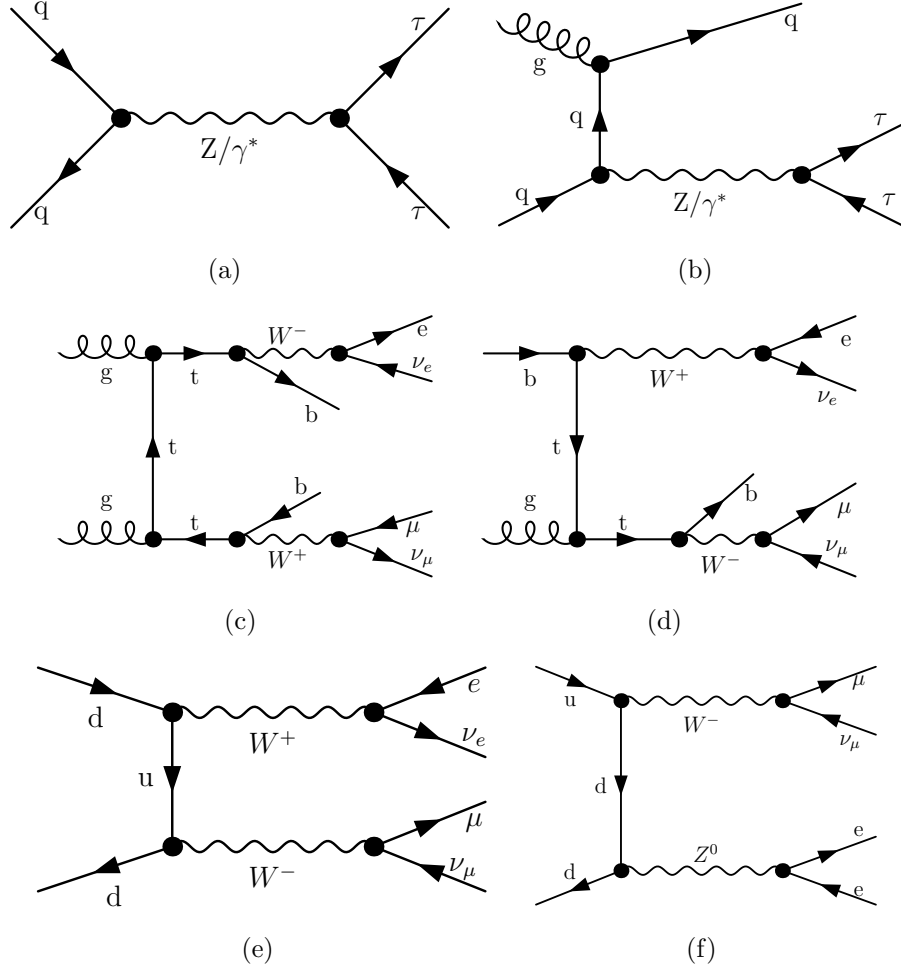


Figure 1.3: Examples of tree level Feynman diagrams for the production and decays of the most relevant backgrounds. The production of $Z/\gamma^* \rightarrow \tau^+\tau^-$ either via Drell-Yan process or in association with jets is shown in (a) and (b), top quark pair and single top quark production in (c) and (d), while examples of WW and WZ production are shown in (e) and (f) respectively.

any b-tagged jets is required, thus searching mainly the signal produced via gluon fusion. The main background process in this category is $Z/\gamma^* \rightarrow \tau\tau$. In contrast, the presence of exactly one b-tagged jet is required in the so called *b-tagged* event category, searching predominantly signal produced in association with b-quarks. The requirement of a b-jet in the final state suppresses the $Z/\gamma^* \rightarrow \tau\tau$ background, consequently, $t\bar{t}$ and single top quark production are the main background processes in this event category. Further selection criteria are introduced in both event categories, these are optimised to enhance the signal produced by the corresponding production mode.

The search is performed within the MSSM m_h^{mod} benchmark scenario scanning the $m_A - \tan\beta$ plane in the ranges $90 \leq m_A \leq 300$ GeV and $5 < \tan\beta < 60$. The prediction of the signal event yields and kinematical distributions are evaluated by simulation. The contribution of the dominant $Z/\gamma^* \rightarrow \tau\tau$ background process is measured in a dedicated signal-depleted control data sample, in order to reduce the systematic uncertainties of the simulation. Similarly, the QCD multi-jet background contribution is also estimated from dedicated data control sample since this background process it is hardly modelled by simulation. Contribution of all other background processes is estimated from simulation. The modelling of the background processes is validated using different signal-depleted validation data samples and good agreement is found.

The systematic uncertainties on cross section calculations and the modelling of the detector response are taken into account for simulated signal and background processes. For background processes that are measured with data, the uncertainties of the corresponding measurement methods are evaluated.

The final statistical interpretation of the data is based on the comparison of the observed $\tau\tau$ invariant mass distributions with the prediction of the background-only and signal-plus-background hypothesis. Exclusion limits on the signal production are set by means of a binned profiled likelihood ratio test statistic. The limits are interpreted within the MSSM m_h^{mod} scenario in terms of the constraints on the m_A and $\tan\beta$ values. Furthermore, the results are also expressed in a less model-dependent way in terms of the upper limits on the cross section for the pro-

duction of a generic Higgs boson ϕ with a mass m_ϕ via the production processes $pp \rightarrow b\bar{b}\phi$ and $gg \rightarrow \phi$.

1.1.4 Data and Simulated Event Samples

Data Sample

The presented result are based on proton-proton collision data recorded by the ATLAS experiment during 2012 at a centre-of-mass energy of $\sqrt{s} = 8$ TeV, corresponding to an integrated luminosity of 20.3 fb^{-1} . The events used in this analysis are recorded using a combination of a single electron and combined electron-muon triggers. Only recorded events in which all relevant components of the ATLAS detector were fully operational are considered. Additional data quality requirements are applied to each event according to [113]. These requirements assure the rejection of events with jet activity in known noisy calorimeter regions.

Signal Samples

Signal production via the gluon fusion process, $gg \rightarrow A/H/h$, was simulated with POWHEG [77] and the associated $b\bar{b}A/H/h$ production with SHERPA [78]. The pseudo-scalar Higgs boson samples were generated in the mass range from 90 GeV to 300 GeV assuming $\tan\beta = 20$, all three neutral Higgs bosons ($A/h/H$) are assumed to decay with the same kinematic properties. Appropriate re-weighting of the production cross sections is applied to simulate other $\tan\beta$ values. The m_h^{mod} MSSM benchmark scenario is assumed.

Background Samples

The production of W and Z/γ^* bosons in association with jets was simulated with the ALPGEN [70] generator. The $t\bar{t}$ process was generated using the POWHEG generator. The single top quark production via s-channel and in Wt process were generated using MC@NLO [72], while single top quark production via t-channel was generated with the AcerMC [73] generator. Diboson processes (WW , WZ , ZZ) were generated with the HERWIG [74] generator. For all ALPGEN

and MC@NLO event samples described above, the parton shower and hadronization were simulated with HERWIG and the underlying event activity with the JIMMY [75] programme. Different sets of parton density functions (PDFs) are used depending on the generator: CTEQ6L1 [79] is used by ALPGEN and AcerMC while CT10 [80] is used by SHERPA, POWHEG and MC@NLO.

TAUOLA [82] and PHOTOS [83] are used to model the tau lepton decay and additional photon radiation from charged leptons in the leading-log approximation, respectively.

The ATLAS detector response is simulated for all generated samples using the GEANT4 [84, 85] package, the reconstruction of physics objects, described in chapter ??, is performed with the same software used also for the data. The effects of the simultaneous recording of additional proton collisions from the same or neighbouring bunch crossings (pile-up) are taken into account in the simulation.

1.2 Event Selection and Categorization

1.2.1 The Common Selection Criteria

According to the characteristic properties of signal events, each event in data and simulation should satisfy the selection criteria described in the following. Since these are shared by both the b-tagged and b-vetoed event category, they are referred to as common selection criteria:

- (i) A trigger selection, requiring the presence of a single electron with $p_T > 24$ GeV, or alternatively, an electron with $p_T > 12$ GeV together with a muon with $p_T > 8$ GeV.
- (ii) At least one reconstructed vertex with more than three associated tracks. This selection is aimed to reject background from cosmic muons.
- (iii) Exactly one reconstructed “Tight” electron with $|\eta| < 1.37$ or $1.52 < |\eta| < 2.47$. The electron should have $p_T > 15$ or 25 GeV depending on the trigger that selected the event.

- (iv) Exactly one “Combined” muon with $|\eta| < 2.5$ and $p_T > 10$ GeV.
- (v) The electron should be isolated with $E_T^{cone}/p_T < 0.08$ and $P_T^{cone}/p_T < 0.06$.
- (vi) The muon should be isolated with $E_T^{cone}/p_T < 0.04$ and $P_T^{cone}/p_T < 0.06$.
- (vii) Muon and electron should be of opposite charge.
- (viii) Overlap removal between electron, muon, τ_h and jets is performed.
- (ix) The event is rejected if at least one hadronic τ lepton decay is found with τ -jet transverse momentum $p_T > 15$ GeV.
- (x) To reduce QCD-multijet background contamination, the invariant mass obtained from the sum of the electron and muon four-momenta should be greater than 30 GeV.

Details on the definition of physics objects and the applied quality criteria can be found in chapter ??.

Events accepted by the common selection criteria are categorized into the *b-tagged* and *b-vetoed* event categories by requiring the presence of exactly one b-tagged jet or the absence of any b-tagged jet in the event, respectively. A jet is considered b-tagged if it has $p_T > 20$ GeV, $|\eta| < 2.5$, $JVF > 0.5$ and it passes the selection of the *MV1* b-tagging algorithm at 70% of efficiency for b-quark, $\epsilon_b^{t\bar{t}}$. Further selection criteria are applied to each category and optimized separately, as described in the following.

1.2.2 b-vetoed Event Category

A veto on the presence of b-tagged jets in the final state allows for the selection of signal events which are produced predominantly via gluon fusion. In this event category the $Z/\gamma^* \rightarrow \tau\tau$ process is an irreducible background due to the same topology of the Higgs and Z boson decay. Other background processes can still be discriminated against the signal due to their kinematic properties. The τ leptons from the Higgs boson decay are highly boosted and so are their decay products,

Category	Selection
b-vetoed	No b-tagged jets $\Delta\phi_{e,\mu} > 1.6$ $\sum \cos \Delta\phi > -0.4$
b-tagged	Exactly one b-tagged jet $\Delta\phi_{e,\mu} > 2$ $\sum \cos \Delta\phi > -0.2$ $H_T < 100 \text{ GeV}$ $P_{T\mu} + P_{Te} + E_T^{miss} < 100 \text{ GeV}$

Table 1.2: Summary of the event selection criteria in the b-tagged and b-vetoed event categories, applied after the common event selection has been performed.

this results in significantly different lepton kinematic with respect to diboson or $t\bar{t}$ background processes. Firstly, the electron and muon from Higgs boson decay will be more likely emitted back-to-back. This is illustrated in Figure 1.4(a), showing the angular distance between the two leptons in the transverse plane $\Delta\phi_{e,\mu} = |\phi_e - \phi_\mu|$ for the signal and relevant background processes. Secondly, the neutrinos from the Higgs boson decay will be more likely collinear with the charged leptons, thus, the angular correlation between the direction of the missing transverse energy and the two leptons, derived as:

$$\hat{E}_T^{miss} \cdot (\hat{P}_T^\mu + \hat{P}_T^e) = \cos(\Delta\phi_{E_T,\mu}) + \cos(\Delta\phi_{E_T,e}) = \sum_{\ell} \cos(\Delta\phi_{E_T,\ell})$$

is expected to tend to zero, as is shown in Figure 1.4(b). These two features can be used to discriminate the signal from the W boson, top quark and dibosons background processes. No further selection criteria are applied in this event category, as it has been shown that no significant improvement of the analysis sensitivity can be achieved. The exact selection criteria are listed in Table 1.2, while in Table 1.3 the predicted number of background and signal events after each stage of selection are reported.

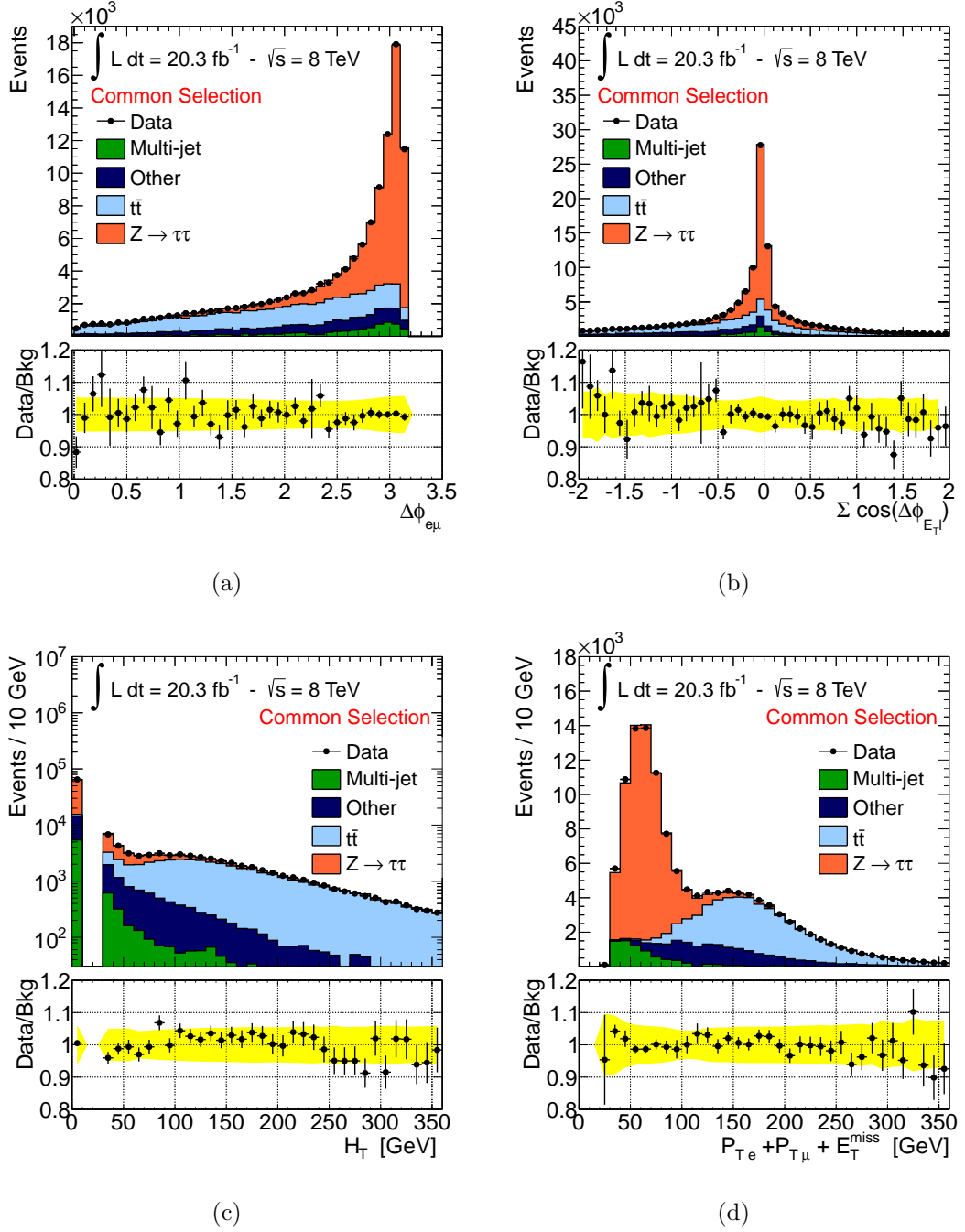


Figure 1.4: Distributions of relevant discriminating variables shown after the common selection has been applied. The prediction of the background model is compared to data. The contribution of the $Z/\gamma^* \rightarrow \tau\tau$ and QCD multi-jet background processes is measured in dedicated signal-depleted control data samples, the prediction for all the other background processes is obtained from simulation. The notation “Other” stands for the electroweak processes $W \rightarrow \ell\nu$, $Z \rightarrow \ell\ell$, diboson and single top quark production. The yellow band represents the total systematic uncertainty for the background model prediction (see Section 1.4).

1.2.3 b-tagged Event Category

The request of exactly one b-tagged jet in the b-tagged event category selects predominantly signal events produced in b-quarks associated production mode. Background processes with b-jet activity, as the top quark and single top quark production become enhanced compared to the $Z/\gamma^* \rightarrow \tau\tau$ background. Also in this category selection requirement on $\Delta\phi_{e,\mu}$ and $\sum \cos \Delta\phi$ are imposed to reduce the top quark and diboson background contributions, as described for the b-vetoed event category. Further selection criteria specific for this category are employed as described below.

Signal events in this event category can be discriminated from the top quark process given their relatively low jet activity. The top quark process is very likely to have two or more highly energetic jets in the event, unlike the signal b-jet which are relatively low energetic. Weak jet activity is ensured by requesting the sum of the jets transverse momenta H_T in the event to be small. The H_T distribution is shown in Figure 1.4(c). The jets used for the calculation of the H_T value should have $p_T > 30$ GeV, $|\eta| < 4.5$ and $JVF > 0.5$ (if $|\eta| < 2.5$).

Another feature that discriminate top quark pair production from the Higgs boson signal is the higher invariant mass of the former final state, as the highest Higgs mass considered for the presented search is 300 GeV. The sum of electron and muon transverse momenta with E_T^{miss} is used as a corresponding discriminating variable, whose distribution is shown in Figure 1.4(d).

The summary of the exact optimized selection criteria for the b-tagged event category is shown in Table 1.2. In Table 1.4 the predicted number of background and signal events after each stage of selection in the b-tagged event category is reported.

1.2.4 Mass Reconstruction with MMC Technique

Accurate invariant mass reconstruction of a di- τ resonance is a challenging task due to the undetected neutrinos. In the presented analysis a total of four neutrinos are involved in the final state, two for each of the τ lepton decays. The invariant mass

	Common Selections	n(b-jet)=0	$\Delta\phi(e - \mu) > 1.6$	$\sum \cos \Delta\phi > -0.4$
Data	125886	89155	-	- -
Multi-jet	6693 ± 456	6357 ± 461	5322 ± 438	4137 ± 339
$Z \rightarrow \ell\ell$	569 ± 48	564 ± 48	516 ± 47	434 ± 44
$W \rightarrow \ell\nu$	1625 ± 155	1604 ± 155	1145 ± 125	714 ± 101
Dibosons	9338 ± 48	9235 ± 48	7358 ± 43	4002 ± 31
$t\bar{t}$	40632 ± 106	7707 ± 46	5044 ± 37	3416 ± 31
Single Top	4449 ± 44	1664 ± 27	1124 ± 22	682 ± 18
$Z/\gamma^* \rightarrow \tau\tau$	61503 ± 68	60440 ± 67	58078 ± 65	55303 ± 64

Table 1.3: Number of observed and predicted signal and background events, after each selection stage in the b-vetoed event category.

depends on eight unknowns given by the two sums of neutrino four-momenta, one for each τ lepton decay. These unknowns can be constrained by four parameters obtained from the measured missing transverse energy and from the τ lepton mass using the following equations:

$$\begin{aligned} \vec{E}_T^{miss} &= \vec{P}_T^{mis_1} + \vec{P}_T^{mis_2} \\ M_{\tau_i}^2 &= m_{mis_i}^2 + m_{vis_i}^2 + 2\mathbf{P}_{vis_i} \cdot \mathbf{P}_{mis_i} \end{aligned} \quad (1.1)$$

where the index i runs over the two τ leptons in the event. $\vec{P}_T^{mis_i}$, m_{mis_i} and \mathbf{P}_{mis_i} are respectively the transverse momentum, the invariant mass and the four momentum of the pair of neutrinos originating from the decay of the i -th τ lepton with mass M_τ . The subscript *vis* indicates instead quantities related to the charged lepton from the corresponding τ lepton decay. The remaining four degrees of freedom can be further constrained, for example, assuming that the neutrinos are collinear to the electron or muon from the corresponding τ lepton decay. This approximation, however, introduces limitations on the mass resolution.

In this analysis, the so-called "Missing Mass Calculator" (MMC) algorithm is used to calculate the most likely invariant mass of the di- τ system for a given event topology. The implementation of the MMC method in this search is based on [129]. The MMC algorithm solves the equations 1.1 for a set of points in a grid of a four-dimensional parameter space. The four independent variables are chosen to be $m_{mis_i}^2$ and $\cos\theta_i^*$, the latter defined as the angle between the charged lepton

	n(b-jet)=1	$\Delta\phi$	$\sum \cos \Delta\phi$	$P_{T\mu} + P_{Te} + E_T^{miss}$	H_T
Data	23352	-	-	-	-
Multi-jet 330 ± 40	208 ± 27	135 ± 22	114 ± 17	100 ± 15	
$Z \rightarrow \ell\ell$	5.2 ± 1.8	2.3 ± 1.1	2.3 ± 1.1	1.7 ± 1.0	0.9 ± 0.8
$W \rightarrow \ell\nu$	20 ± 6	15 ± 6	13 ± 6	10 ± 6	10 ± 6
Dibosons	99 ± 5	63 ± 4	36.4 ± 3.0	14.8 ± 1.8	13.3 ± 1.8
$t\bar{t}$	19810 ± 70	9680 ± 50	6450 ± 50	808 ± 15	350 ± 10
Single Top	2456 ± 33	1223 ± 23	784 ± 18	122 ± 7	99 ± 7
$Z/\gamma^* \rightarrow \tau\tau$	952 ± 9	625 ± 7	540 ± 7	482 ± 6	421 ± 6

Table 1.4: Number of observed and predicted signal and background events, after each selection stage in the b-tagged event category.

from the τ lepton decay and the boost direction of the τ lepton. The di- τ invariant mass in each event is then calculated for each given point of the parameter space. Each solution is weighted by the probability that a τ lepton decay assumes a given configuration. The probability of a given configuration is predicted by means of simulation using PYTHIA generator supplemented with TAUOLA package. The invariant mass of the di- τ system, $m_{\tau\tau}^{MMC}$, is then defined as the maximum of the weighted invariant mass distribution obtained from all scanned points.

The resolution of the missing transverse energy measurement impacts the resolution of the invariant mass obtained with the $m_{\tau\tau}^{MMC}$ method. To improve the E_T^{miss} resolution, a scan over a six-dimensional parameter space is performed in a similar manner as described above. For this purpose, the value of \vec{E}_T^{miss} is also considered unknown and a scan is performed over all possible values constrained by the measured E_T^{miss} and its corresponding uncertainty.

Figure 1.5 shows the $m_{\tau\tau}^{MMC}$ invariant mass distribution after the common selection and after the requirement of the presence or the absence of a b-tagged jet.

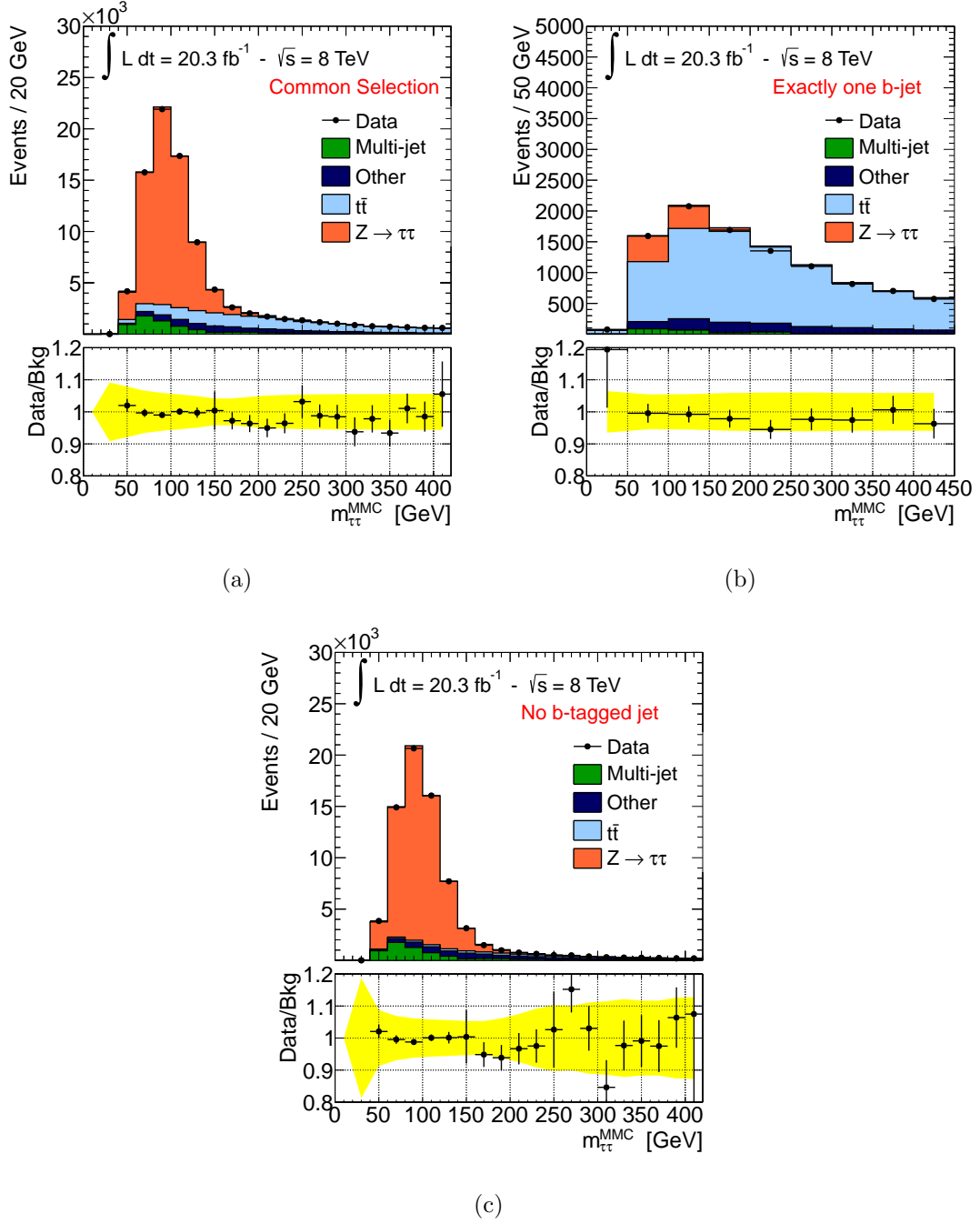


Figure 1.5: Observed and expected distribution of the invariant di- τ mass $m_{\tau\tau}^{MMC}$ for different stage of analysis selections: after requiring the common selection (a), additionally requiring the presence of exactly one b-tagged jet (b) or the absence of a b-tagged jet (c). The prediction of the background model is compared to data. The contribution of the $Z/\gamma^* \rightarrow \tau\tau$ and QCD multi-jet background processes is measured in dedicated signal-depleted control data samples, the prediction for all the other background processes is obtained from simulation. The notation “Other” stands for the electroweak processes $W \rightarrow \ell\nu$, $Z \rightarrow \ell\ell$, diboson and single top quark production. The yellow band represents the total systematic uncertainty for the background model prediction.

1.3 Background Prediction and Validation

This section describes the strategies for the prediction of the background contributions and validation of these predictions. Monte Carlo simulation is extensively used to model the kinematic properties of the background and signal processes. However, since the simulation of any process is usually prone to systematic uncertainties due to a non-perfect description of the pileup effects, underlying event and detector performance, the background contributions from $Z/\gamma^* \rightarrow \tau\tau$ and QCD multi-jet process are estimated using dedicated signal-free control data samples, as described respectively in section 1.3.3 and 1.3.2. Contributions of other background processes, such as $t\bar{t}$, single top quark, dibosons, $Z \rightarrow ll + \text{jets}$ (where $l = e, \mu$) and $W + \text{jets}$, are estimated from simulation. Given the relatively large $t\bar{t}$ background contribution, a dedicated study to validate this background prediction has been made as described in section 1.3.1.

A good agreement between data and background prediction is found after the common selection, as can be seen in Figure 1.4 and Figure 1.6.

1.3.1 Validation of the $t\bar{t}$ Background Prediction

The background contribution from top quark pair production is estimated using a sample of simulated events generated with POWHEG-PYTHIA Monte Carlo generator. Since this is one of the major background processes for the presented analysis a careful validation of the predicted contribution is needed. For this purpose signal-depleted data validation sample enriched with $t\bar{t}$ events by requiring the presence of exactly two b-tagged jets in all the events passing the common selection is employed. Figures 1.7 and 1.8 show the distributions for a set of kinematic properties and all discriminating variables obtained with this data sample. Good agreement between data and Monte Carlo prediction is found with overall ratio of the observed to the predicted number of $t\bar{t}$ events of $0.998 \pm 0.011(\text{stat.}) \pm 0.110(\text{sys.})$. The total systematic uncertainty on the ratio is dominated by the uncertainty of the b-tagging efficiency.

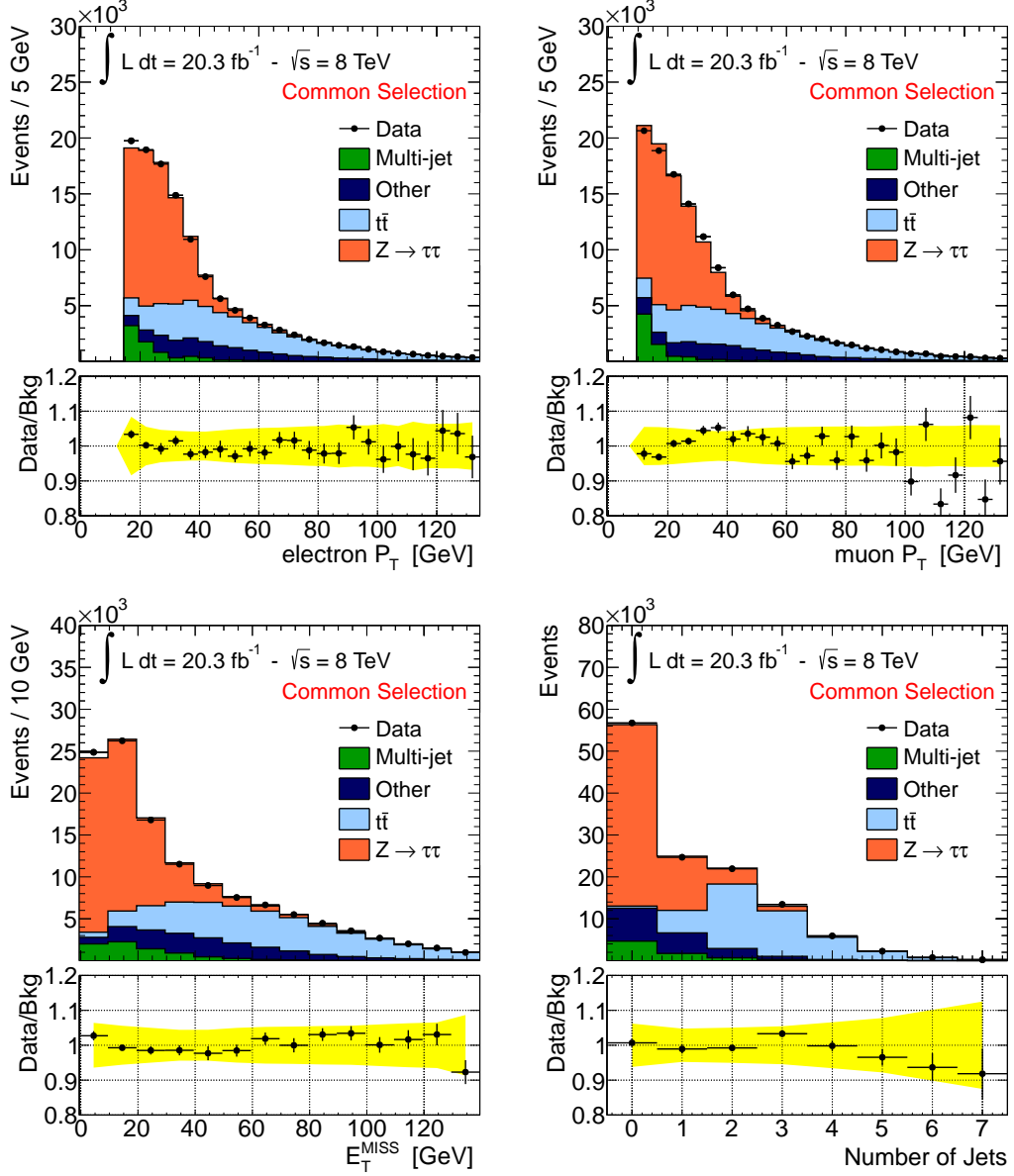


Figure 1.6: Observed and expected distribution of kinematic variables after common selections. The prediction of the background model is compared to data. The contribution of the $Z/\gamma^* \rightarrow \tau\tau$ and QCD multi-jet background processes is measured in dedicated signal-depleted control data samples, the prediction for all the other background processes is obtained from simulation. The notation “Other” stands for the electroweak processes $W \rightarrow \ell\nu$, $Z \rightarrow \ell\ell$, diboson and single top quark production. The yellow band represents the total systematic uncertainty for the background model prediction.

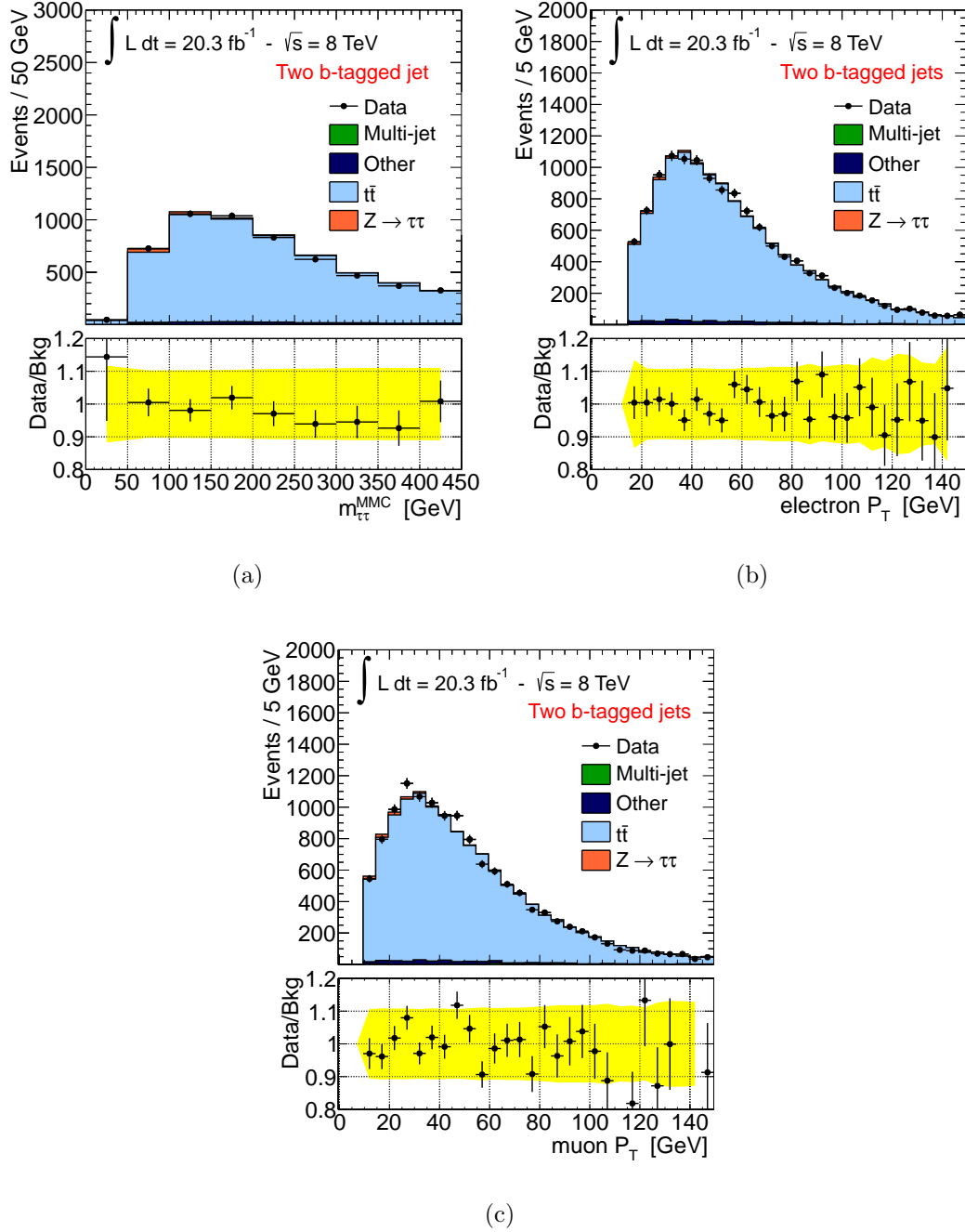


Figure 1.7: Observed and expected distributions of (a) the di- τ invariant mass $m_{\tau\tau}^{MMC}$, (b) the electron transverse momentum and (c) the muon transverse momentum in the $t\bar{t}$ validation sample. The contribution of the $Z/\gamma^* \rightarrow \tau\tau$ and QCD multi-jet background processes is measured in dedicated signal-depleted control data samples, the prediction for all the other background processes is obtained from simulation. The notation “Other” stands for the electroweak processes $W \rightarrow \ell\nu$, $Z \rightarrow \ell\ell$, diboson and single top quark production. The error bars on the observed to the predicted events ratio indicates the statistical uncertainty, whereas the yellow band indicates the total systematic uncertainty of this ratio.

Data Sample	Relative Lepton Charge	Lepton Isolation
A (signal sample)	OS	isolated
B	SS	isolated
C	OS	anti-isolated
D	SS	anti-isolated

Table 1.5: Control data samples for the measurement of the QCD multi-jet background contribution. The samples are defined by the requirements on the relative charge sign of the two leptons (OS,SS) and the isolation criteria applied on them (isolated or anti-isolated). See text.

1.3.2 Multi-jet Background Measurement

The QCD multi-jet process represents an important background, especially in the b-vetoed event category, due to its high cross-section and the relatively low threshold on the lepton p_T used in this analysis. The contribution of this background is evaluated by the so-called ABCD data-driven technique. The ABCD method splits the sample of data events after the common selection into four sub-samples: the signal sample (A), defined by the event selections criteria described in Section 1.2 and three signal-depleted control data sample (B,C,D), which are orthogonal to each other and are enriched in multi-jets events. The three control data samples are defined by inverting the requirements on the relative sign of the electron and muon charge and on the isolation criteria. Both the calorimetric and tracking isolation criteria described in Section 1.2.1 are inverted for each electron and muon with respect to the nominal values, thus defining the so-called anti-isolated leptons. The data are divided into four samples of events with leptons of opposite sign charge (OS) or same sign charge (SS) with respectively isolated or anti-isolated leptons, as summarized in Table 1.5.

The ABCD method assumes that there is no correlation between the relative charge and lepton isolation in QCD multi-jet events, or in other words that the ratio of OS/SS events is uncorrelated with the lepton isolation criteria. In this case, the number (N_A) of QCD multi-jet events in the signal sample A can be

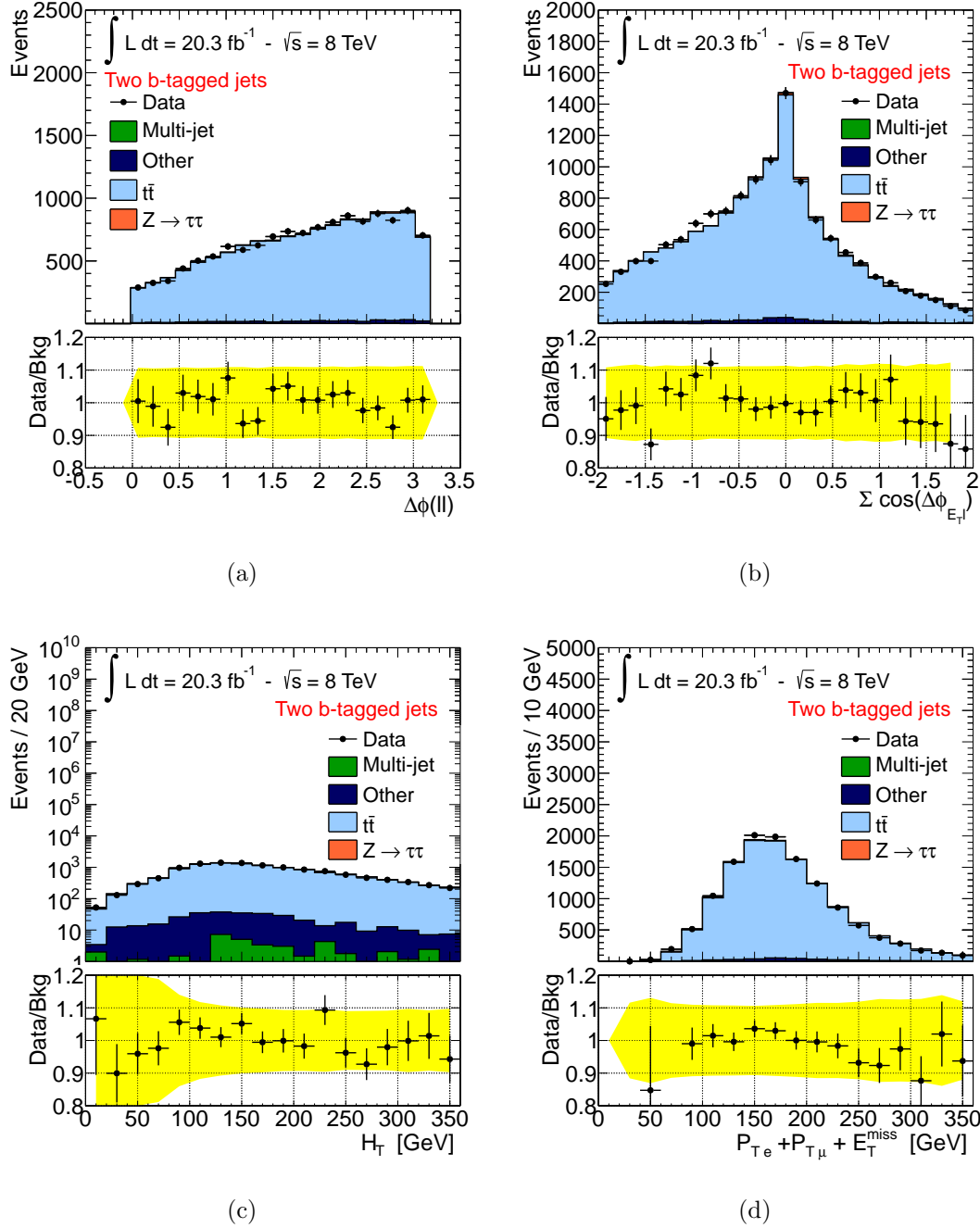


Figure 1.8: Observed and expected distributions of the discriminating variables, (a) $\Delta\phi(e - \mu)$, (b) $\sum \cos \Delta\phi$, (c) $p_{T\mu} + p_{Te} + E_T^{miss}$ and (d) H_T in the $t\bar{t}$ validation sample. The background prediction is performed as previously stated. The error bars on the observed to the predicted events ratio indicates the statistical uncertainty, whereas the yellow band indicates the total systematic uncertainty of this ratio.

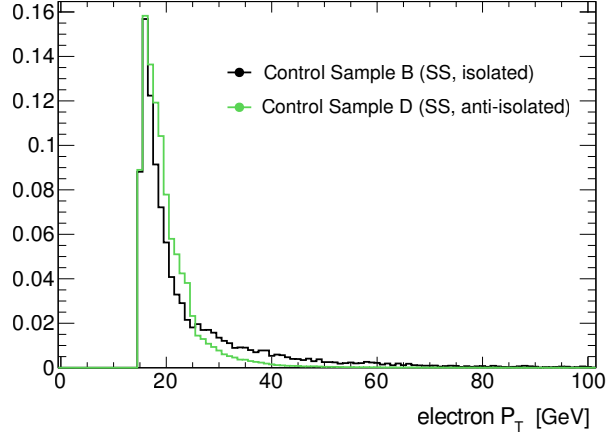


Figure 1.9: Comparison of the electron p_T distribution in control samples B and sample D, showing the bias due to the trigger. The histograms are normalized to the same area.

estimated from the yields (N_B , N_C , N_D) of multi-jet events in the control samples B , C and D , using the equation

$$N_A = N_B \times \frac{N_C}{N_D} = N_B \times R_{QCD} \quad (1.2)$$

To obtain the pure QCD multi-jet event yields in the data control samples, the contribution from contaminating electroweak (W +jets, Z +jets and dibosons) and top quark processes ($t\bar{t}$, single top quark production) is subtracted in each control sample based on the prediction from simulation. Tables 1.7 and 1.6 show the observed event yield in each control sample at different stages of the event selection along with the predictions of non-QCD background contributions which are subtracted. Signal contamination has been evaluated in all three control samples for different signal mass points. For the range of m_A and $\tan\beta$ values considered in this analysis, the highest signal contamination is seen in sample B for the mass point $m_A = 300$ GeV and $\tan\beta = 50$, where a contamination of 0.2% is observed².

The modelling of the shapes of kinematic distributions in QCD multi-jet events

² This contamination signal originates mainly from the production in association with b-quarks and, as it scales with the cross section, it will be an order of magnitude smaller for $\tan\beta = 20$.

is given by the data sample B. The events in this sample are expected to have similar kinematic properties as in the signal sample. A drawback of this choice is a rather low number of events and a higher contamination with non-QCD process compared to samples C and D. Sample B is chosen to avoid a shape bias due to isolation requirements at the trigger level, since the single-electron trigger already imposes isolation requirements. Figure 1.9 shows the comparison of the electron p_T distributions in sample B and D. In the latter sample high- p_T electrons are suppressed as they do not pass the trigger selection. Eventually the trigger isolation requirement could also bias the ratio R_{QCD} . This possibility has been carefully studied in a dedicated study as reported in Appendix A. To a good approximation, the mentioned trigger effects cancel out in the ratio R_{QCD} and no additional systematic uncertainty needs to be taken into account.

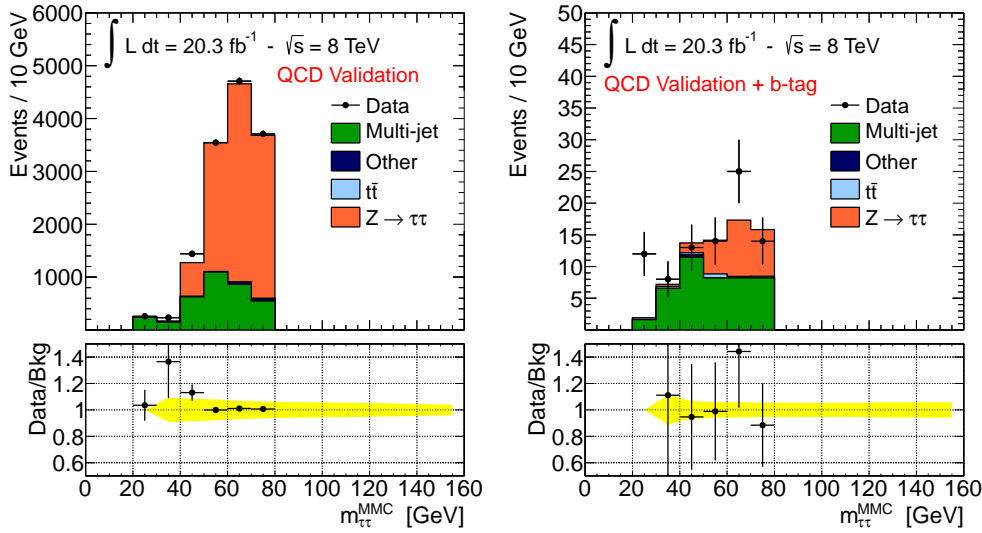


Figure 1.10: $m_{\tau\tau}^{MMC}$ distribution obtained with QCD validation samples defined in Section 1.3.2, without (left) and with an additional requirement of exactly one b-tagged jet in the final state (right). The error bars and the yellow band indicates the statistical and systematic uncertainty respectively.

To test the predictions of the ABCD method an additional validation sample has been defined with the following selection criteria after applying the common

Event Selection		B	C	D	R_{QCD}
Common Selection	Data	6189	604628	312901	1.929 ± 0.004
	non-QCD	2510 ± 180	1090 ± 30	730 ± 35	
B-veto	Data	5673	558217	284847	1.960 ± 0.004
	non-QCD	2220 ± 180	710 ± 30	415 ± 30	
$\Delta\phi_{e,\mu}$	Data	4610	532583	271404	1.962 ± 0.005
	non-QCD	1700 ± 170	580 ± 30	345 ± 30	
$\sum \cos \Delta\phi$	Data	3417	486747	247712	1.965 ± 0.005
	non-QCD	1120 ± 100	370 ± 20	230 ± 20	
$m_{\tau\tau}^{MMC} > 0.$	Data	3177	479967	244276	1.965 ± 0.005
	non-QCD	1000 ± 100	300 ± 17	190 ± 20	

Table 1.6: Number of observed events and the predicted non-QCD contribution at different stages of the event selections for b-veto category. The error on the R_{QCD} ratio is of statistical nature only.

selection:

- $E_T^{miss} < 20$ GeV
- $H_T < 70$ GeV and $p_{T\mu} + p_{Te} + E_T^{miss} < 50$ GeV
- $0 < m_{\tau\tau}^{MMC} < 80$ GeV

This validation sample is designed to enhance the multi-jet background contribution with respect to $Z/\gamma^* \rightarrow \tau\tau$ keeping the final state kinematics as similar as possible to the signal sample. Figure 1.10 shows the $m_{\tau\tau}^{MMC}$ distribution for this validation sample with and without the b-tagging requirements. Agreement between data and the background predictions is found within statistical and detector-related systematics uncertainty.

Systematic uncertainties are assigned on the scaling factor R_{QCD} and on the shape of the discriminating variable $m_{\tau\tau}^{MMC}$ to take into account any correlation between the isolation and the relative charge of the leptons as detailed in Section 1.4.

Event Selection		B	C	D	R_{QCD}
Common Selection	Data	6189	604628	312901	1.929 ± 0.004
	non-QCD	2510 ± 180	1090 ± 30	730 ± 35	
B-tag	Data	419	44619	27257	1.64 ± 0.01
	non-QCD	215 ± 10	310 ± 12	277 ± 13	
$\Delta\phi_{e,\mu}$	Data	230	38810	23316	1.67 ± 0.01
	non-QCD	104 ± 6	200 ± 10	175 ± 7	
$\sum \cos \Delta\phi$	Data	149	31379	18779	1.67 ± 0.02
	non-QCD	67 ± 5	127 ± 8	114 ± 6	
$\sum H_T$	Data	83	27781	15626	1.78 ± 0.02
	non-QCD	23 ± 4	25 ± 3	22 ± 3	
$p_{T\mu} + p_{Te} + E_T^{miss}$	Data	71	27735	15590	1.78 ± 0.02
	non-QCD	10 ± 3	22 ± 3	18 ± 2	
$m_{\tau\tau}^{MMC} > 0.$	Data	70	27634	15522	1.78 ± 0.02
	non-QCD	9 ± 3	20 ± 3	17 ± 2	

Table 1.7: Number of observed events and the predicted non-QCD contribution at different stages of the event selections for b-tag category. The error on the R_{QCD} ratio is of statistical nature only.

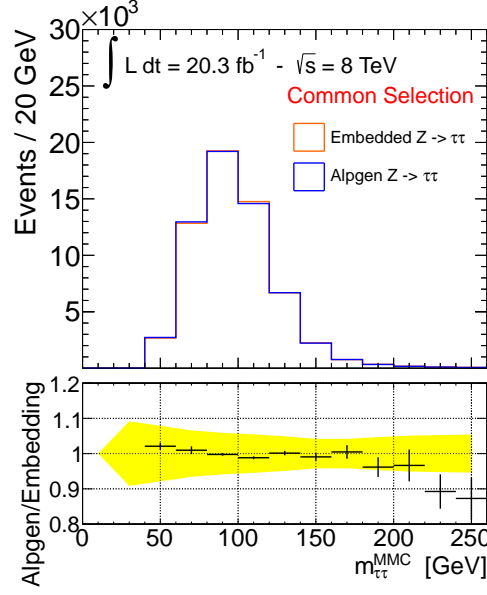


Figure 1.11: Comparison of the $m_{\tau\tau}^{MMC}$ distributions obtained from the ALPGEN $Z/\gamma^* \rightarrow \tau\tau$ simulation and from the embedding technique after the requirements of the common selection has been applied. The yellow band indicates the total systematic uncertainty relative to the ALPGEN simulation sample.

1.3.3 $Z \rightarrow \tau\tau + \text{Jets}$ Background Measurement

The $Z/\gamma^* \rightarrow \tau\tau$ decays are the major source of background to the presented analysis, calling for its thorough understanding. Unfortunately, for a light Higgs boson, it is impossible to fully discriminate the $Z/\gamma^* \rightarrow \tau\tau$ decays from the signal and thus a dedicated signal-free data control sample cannot be defined. However, thanks to the small Higgs boson coupling to muons, $Z \rightarrow \mu\mu$ decays provide a good starting point to model $Z/\gamma^* \rightarrow \tau\tau$ events based on data. A hybrid approach relying on data and simulation known as the "embedding" is used for this purpose. The $Z \rightarrow \mu\mu$ event candidates are selected in data. The two muons from the Z decay are then substituted with the decay products from simulated τ lepton decays. The energy deposit in the calorimeter and the reconstructed tracks in a cone of given size around the muon are subtracted and substituted with the

corresponding predictions from the τ lepton decay. These τ leptons have the same kinematic properties as the original muons. Further details on the embedding technique may be found in [86, 87].

As the Trigger is not simulated in the described embedded samples, only the shapes of kinematic distributions are modelled by the embedded sample, while the $Z \rightarrow \tau\tau$ event yield is normalized to ALPGEN $Z/\gamma^* \rightarrow \tau\tau$ prediction at the common selection stage. Furthermore, a set of corrections as described in [88], is applied to unfold from the original $Z \rightarrow \mu\mu$ trigger and reconstruction efficiency. Subsequently, the trigger and reconstruction efficiency of the $e\mu + 4\nu$ final state are emulated by means of event weights.

The embedding technique has been validated in several studies detailed in [86, 88], demonstrating a reliable performance of the embedding technique and a good description of data. Figure 1.11 shows a comparison of the $m_{\tau\tau}^{MMC}$ distribution between embedded and ALPGEN $Z/\gamma^* \rightarrow \tau\tau$ events, no significant differences are seen. Other relevant discriminating variables, such as the E_T^{miss} and the number of b-jets in the final state, are instead slightly better described by the embedded $Z/\gamma^* \rightarrow \tau\tau$ sample, as shown in Figure 1.12, this behaviour is expected due to the imperfect modelling of these variables with simulation.

The embedded sample is based on the selected $Z \rightarrow \mu\mu$ event candidates in data. The $Z \rightarrow \mu\mu$ selection criteria assure a rather pure $Z \rightarrow \mu\mu$ sample. However, further event selection criteria used in the presented analysis, for example the b-tagging requirements, could enhance the contamination of this sample with events from other processes. Dedicated studies have been made to estimate the $t\bar{t}$ and QCD multi-jet contamination in the embedded sample. The $t\bar{t}$ contamination is estimated by evaluating the yield of embedded $Z \rightarrow \tau\tau$ events in a validation sample with two b-tagged jets (as described in Section 1.3.1). These events are assumed to originate solely from the $t\bar{t}$ process and the corresponding yield in the signal sample is extrapolated from simulation. Table 1.8 summarises the evaluated top quark contamination in the embedded $Z \rightarrow \tau\tau$ sample, separately for the two event categories. The multi-jet contamination can be estimated starting from the yield of embedded events in the sample C defined by the ABCD method. It is

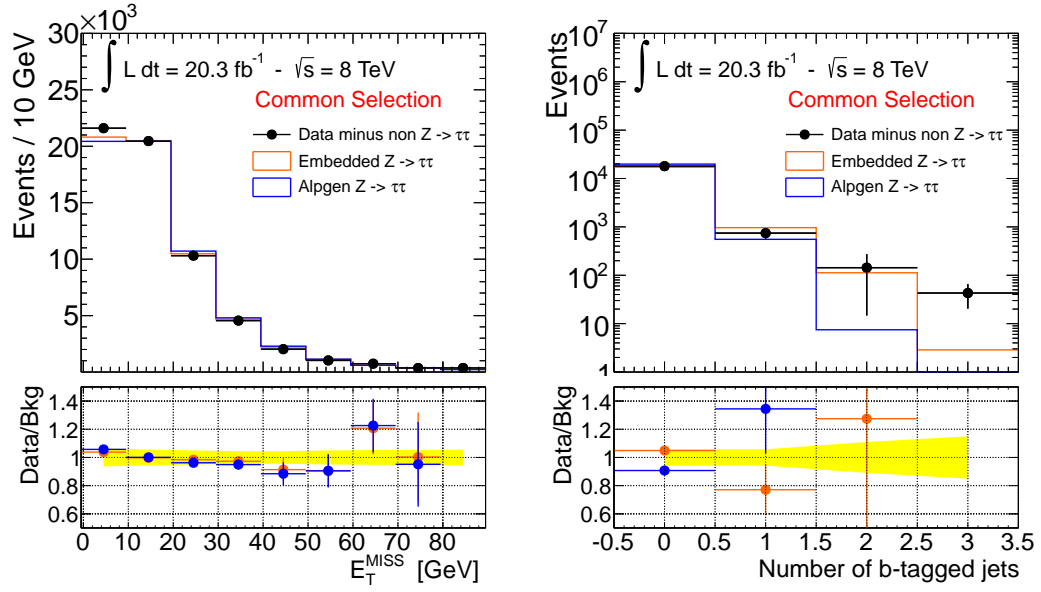


Figure 1.12: Comparison of the (left) E_T^{miss} and (right) b-tagged jet multiplicity distributions in embedded and ALPGEN $Z/\gamma^* \rightarrow \tau\tau$ events after the requirements of the common selection has been applied. Data are superimposed after subtracting the contribution of non- $Z/\gamma^* \rightarrow \tau\tau$ processes. The yellow band indicates the total systematic uncertainty relative to the ALPGEN simulation sample.

assumed that all events in this validation sample are QCD multi-jet events. The QCD multi-jet contamination of the embedded events in the signal sample can be estimated as:

$$N_A^{QCD-emb} = N_C^{QCD-emb} \times \frac{N_B^{\mu\mu}}{N_D^{\mu\mu}} = N_B \times R_{QCD}^{\mu\mu} \quad (1.3)$$

The transfer factor $R_{QCD}^{\mu\mu}$, is evaluated using a di-muon final state with same kinematic selection criteria as for $Z \rightarrow \mu\mu$ candidates entering the embedding procedure. Table 1.9 shows the estimated contamination of QCD multi-jet in the embedded sample. Contamination effects are considered negligible.

	Embedded event yield in $t\bar{t}$ control sample	Transfer factor	Estimated events in signal sample	Contamination
b-tagged	84 ± 9	$(2.6 \pm 0.1) \times 10^{-2}$	2.2 ± 0.2	0.5 %
b-vetoed	84 ± 9	$(1.74 \pm 0.02) \times 10^{-1}$	15 ± 2	0.03 %

Table 1.8: Evaluation of the $t\bar{t}$ contamination in the embedded $Z \rightarrow \tau\tau$ sample using a two b-tag validation sample. The transfer factor is a multiplicative factor obtained from simulation that allows to extrapolate the measurement from the validation sample into the signal sample.

	Embedded event yield in QCD control sample C	Transfer factor	Estimated events in signal sample	Contamination
B-tag	12 ± 3	$(7 \pm 1) \times 10^{-3}$	$(8.4 \pm 0.3) \times 10^{-2}$	0.03 %
B-veto	390 ± 20	$(2.5 \pm 0.1) \times 10^{-2}$	10.0 ± 0.5	0.02 %

Table 1.9: Evaluation of the QCD multi-jet contamination in the embedded $Z \rightarrow \tau\tau$ sample using the control sample with OS anti-isolated events (sample C). The transfer factor $R_{QCD}^{\mu\mu}$ is the multiplicative factor that allows to extrapolate the measured events in control sample C into the signal sample.

1.4 Systematic Uncertainties

This section describes a number of sources of systematic uncertainties that are relevant for the presented analysis. To account for differences in the observed and simulated detector response a set of corrections is applied at the level of object reconstruction and at event level as described in chapter ?? . The uncertainties due to such corrections are referred to as detector-related systematic uncertainties and are addressed in section 1.4.1. For all processes whose contributions are predicted from simulation, also theory-related systematic uncertainties need to be accounted for. These include uncertainties on the cross-section and on the acceptance of events after the given analysis selection criteria and are described in section 1.4.2 . Further systematic uncertainties related to the background measurements with dedicated control data are described in Sections 1.4.3 and 1.4.4 .

Each source of systematic uncertainty can contribute separately to the uncertainty on the final event yield and on the shape of the $m_{\tau\tau}^{MMC}$ distribution which is used as final discriminating variable in the statistical interpretation of data. Systematic uncertainties that affect the shape of the mass distribution are documented in appendix C.3. Uncertainty on the $m_{\tau\tau}^{MMC}$ shape distribution are found to be negligible for all except the embedded sample, for which significant deviation from the nominal distribution are found in the b-vetoed category only. Systematic uncertainties that do not affect the shape of the mass distribution and have an impact on the event yield of less than 0.5% for each process are neglected.

1.4.1 Detector-related Systematics Uncertainties

Systematic uncertainties related to object reconstruction and event-by-event corrections are based on the calibration measurements of the relevant parameter. Each of those parameters correspond to a nuisance parameter in the probability model used for the statistical interpretation as described in Section 1.5. Each parameter is varied independently by one standard deviation according to its measured uncertainty. The corresponding impact on the yield of simulated events is evaluated for each signal and background sample. In the following, detector-related uncertainty

are described in more details. Tables 1.11 and 1.10 briefly summarize the impact of these uncertainties on the predicted sample yields.

Luminosity The integrated luminosity of the 8 TeV data recorded with the ATLAS detector during 2012 is measured to be 20.3 fb^{-1} [63] with an uncertainty of 2.8%.

Pileup Simulated events are re-weighted to reproduce the average number of interactions per bunch crossing $\langle \mu \rangle$ as seen in data. Those event weights have an uncertainty which is propagated to each simulated sample.

Trigger Efficiency is corrected in simulation to match (on the average) the one observed in data. Those correction weights are evaluated as a function of p_T and η of the corresponding leptons and have associated uncertainties. Systematic uncertainties on both the single electron and electron-muon trigger efficiency are taken into account independently and range approximately from 1-2%.

In the embedded $Z \rightarrow \tau\tau$ sample, the trigger is emulated by applying weights according to the event topology. Those weights are related to the ones described above and have similar uncertainties. Trigger efficiency uncertainty for the embedded sample are considered uncorrelated with those of other samples.

Electrons Two sources of uncertainty on reconstructed electron objects are considered: the first related to electron identification and reconstruction efficiencies ("Electron ID"), the second related to electron energy scale and resolution corrections. The energy scale uncertainties are described by a set of six different nuisance parameters [101]. However, only a few of them give a non-negligible contribution to the analysis. Two of them are found to affect the shape of the $m_{\tau\tau}^{MMC}$ distribution and are considered independently: uncertainty arising from the electron momentum measurement with $Z \rightarrow ee$ data ("Electron Zee") and the one related to low momentum electrons ("Electron LOWPT"). All other uncertainties related to energy scale and resolution are summed in quadrature ("Electron E").

Muons The uncertainty on muon identification efficiency depends on the charge and momentum of the muon. Typically these uncertainties are of the order of a fraction of percent, and are referred as "Muon ID". The uncertainties on the muon energy scale and resolution are considered independently for the inner detector and muon spectrometer measurements and are then added in quadrature to estimate the final uncertainty ("Muon E").

Taus-Jets The jets from the hadronically decaying τ leptons are only considered in the analysis by applying a veto on their presence in an event. Uncertainties on both τ -jet energy scale and identification efficiency have been investigated and are found to be negligible for this analysis.

Jets The systematic uncertainties on the Jet Energy Scale (JES) are described by multiple sets of nuisance parameters [112] related to different effects and jet energy components, for example the sensitivity to pileup effects or to the flavour composition of the jet. The overall uncertainty on the JES ranges between 3% and 7%, depending on the p_T and η of the jet. The overall impact of the JES uncertainty on the analysis yields is shown in Tables 1.11 and 1.10 by summing all component in quadrature, while in the statistical interpretation of data those uncertainties are considered uncorrelated. Systematic uncertainty due to the jet resolution ("Jet Resolution") are obtained by smearing the jet energy according to the measured uncertainty which ranges from 10-20% depending on the direction of the jet.

b-Tagging Corrections are applied to simulation to match the b-tagging efficiency observed in data. Uncertainties on the knowledge of the b-tagging efficiencies for the 70% $\epsilon_b^{t\bar{t}}$ working point of the MV1 b-tagger are considered [116, 117]. These uncertainties range from 5-10% in dependence on the p_T of the jet. The effect of those uncertainties is evaluated independently for the b-quark, c-quark and light or gluon initiated jets and referred to respectively as "B Eff", "C Eff" and "L Eff". The tagging and mis-tagging efficiency uncertainties are considered to be fully anti-correlated.

Missing Transverse Energy The effect of the energy scale uncertainties for all physics objects is propagated to the E_T^{miss} calculation. In addition, uncertainty on the energy scale and resolution due to the remaining unassociated calorimeter energy deposits, the “soft-terms”, is considered and estimated to be of the order of 10% [118]. E_T^{miss} uncertainties are independently propagated through the analysis and are added in quadrature, this final term is referred to as the “MET” uncertainty.

1.4.2 Theoretical Uncertainties

Uncertainties on the cross-sections that have been used to normalize the contribution of simulated samples to the integrated luminosity of analyzed data are reported in Table 1.12. These uncertainties include contributions due to parton distribution functions (PDFs), the choice of the value of the strong coupling constant, the renormalisation and factorisation scales. Furthermore, the uncertainties on the signal cross-section depend on the $\tan\beta$ value, the nature of the Higgs boson ($A/h/H$) and its mass.

The impact of systematic uncertainties due to various Monte Carlo tuning parameters for the description of the underlying event and lepton kinematic properties is considered. Since the distribution of the invariant mass of all visible τ lepton decay products is found to be not affected by these systematic, uncertainties only the variation in the acceptance is considered as a systematic uncertainty. The acceptance uncertainties for the simulated ALPGEN $Z/\gamma^* \rightarrow \tau\tau$ sample, which is used for the normalization of the embedded sample, are estimated at the common selection stage to be 4% [136]. Since additional selection criteria are applied directly to the embedded sample, no further acceptance uncertainties are considered. Acceptance uncertainties on the yield of $t\bar{t}$ simulated events are estimated to be 2% [137]. The acceptance uncertainties on dibosons and single top quark production are estimated to be 2% [136].

Uncertainties on the signal acceptance have been estimated with signal samples produced varying generator parameters. The impact on the selection of leptons, τ -jet and jets is evaluated at the particle level, prior to simulation of the detector

b-vetoed event category, Uncertainties on event yields (%)					
Source	Signal bbH	Signal ggH	$Z/\gamma^* \rightarrow \tau\tau$	Top	Other
Electron ID	2.4	2.3	2.9 (s)	1.4	1.6
Electron E.	0.4	0.5	0.4	0.5	0.9
Electron LOWPT	0.3	0.5	0.4 (s)	0.0	1.2
Electron Zee	0.4	0.4	0.4 (s)	0.1	0.3
Muon ID	0.3	0.3	0.3	0.3	0.3
Muon E.	0.1	0.1	0.1	0.5	0.5
Trigger Single Ele.	0.6	0.6	0.5	0.9	0.9
Trigger Dilep.	1.0	1.0	1.3	0.2	0.3
Embedding MFS	-	-	0.1 (s)	-	-
Embedding Iso.	-	-	0.0 (s)	-	-
JES	0.6	0.7	-	1.0	1.2
JER	0.5	0.3	-	0.6	0.3
B Eff	1.8	0.0	-	12.0	0.8
C Eff	0.0	0.1	-	0.1	0.0
L Eff	0.0	0.1	-	0.2	0.1
Pileup	0.5	0.8	0.4	0.3	0.3
MET	0.2	0.8	0.1	0.2	0.5
Luminosity	2.8	2.8	2.8	2.8	2.8

Table 1.10: Impact of the experimental systematic uncertainties on the event yields in different simulated samples in the b-vetoed event category. Here "Other" refers to the sum of all remaining background samples: $W \rightarrow \ell\nu$, dibosons, $Z \rightarrow \ell\ell$ and single top quark processes. The signal produced in association with b-quarks and via gluon fusion is considered separately assuming $m_A = 150$ GeV and $\tan\beta = 20$. Uncertainty that impacts the $m_{\tau\tau}^{MMC}$ mass distribution are noted with the symbol (s).

b-tagged event category, Uncertainties on event yields (%)					
Source	Signal bbH	Signal ggH	$Z/\gamma^* \rightarrow \tau\tau$	Top	Other
Electron ID	2.3	2.6	2.8	1.8	2.0
Electron E	0.7	1.2	0.5	0.5	0.9
Electron LOWPT	0.4	0.0	0.4	0.1	0.4
Electron Zee	0.3	0.6	0.4	0.6	0.5
Muon ID	0.3	0.3	0.3	0.3	0.3
Muon E	0.5	0.8	0.1	0.1	0.2
Trigger Single Ele.	0.7	0.5	0.5	0.8	0.8
Trigger Dilepton	1.0	1.2	1.4	0.6	0.6
Embedding MFS	-	-	0.0	-	-
Embedding Iso.	-	-	1.3	-	-
JES	2.7	7.3	-	10.0	7.0
JER	1.4	6.3	-	2.9	3.0
B Eff	10.2	3.1	-	2.6	5.0
C Eff	0.2	4.3	-	0.0	1.2
L Eff	0.4	8.0	-	0.1	1.2
Pileup	0.4	0.7	0.4	0.4	0.9
MET	0.7	0.5	0.2	1.0	1.2
Luminosity	2.8	2.8	2.8	2.8	2.8

Table 1.11: Impact of the experimental systematic uncertainties on the event yields in different simulated samples in the b-tagged event category. Here "Other" refers to the sum of all remaining background samples: $W \rightarrow \ell\nu$, dibosons, $Z \rightarrow \ell\ell$ and single top quark processes. The signal produced in association with b-quarks and via gluon fusion is considered separately assuming $m_A = 150$ GeV and $\tan\beta = 20$.

Generator	Process	Uncertainty
ALPGEN	$Z \rightarrow \tau\tau/ee/\mu\mu$	$\pm 5\%$
POWHEG	$t\bar{t}$	$\pm 5.5\%$
ALPGEN	$W \rightarrow \tau\nu/e\nu/\mu\nu$	$\pm 5\%$
AcerMC	single top	$\pm 13\%$
HERWIG	dibosons	$\pm 6\%$
SHERPA	$bbA/h/H$ ($m_A \geq 120$ GeV)	$-(< 20)\%, +(< 9) \%$
SHERPA	$bbA/h/H$ ($m_A = 110$ GeV)	$-(< 25)\%, +(< 9) \%$
SHERPA	$bbA/h/H$ ($m_A = 100$ GeV)	$-(< 28)\%, +(< 9) \%$
SHERPA	$bbA/h/H$ ($m_A = 90$ GeV)	$-(< 30)\%, +(< 9) \%$
POWHEG	$ggA/h/H$ ($m_A \leq 300$ GeV)	$< 15\%$

Table 1.12: Cross-section uncertainties for background and signal processes, $\tan\beta = 20$ is assumed for all signal samples.

response. This truth-level study is implemented within the Rivet framework [139], where the b-tagging is performed by identifying the b-quarks and applying weights according to the measured ATLAS b-tagging efficiencies [116]. The variation of the acceptance with respect to the nominal Monte Carlo tune has been considered as a source of systematic uncertainty. For signal a total acceptance uncertainty varies from 4% to 30% depending on M_A , production process and on the analysis category.

1.4.3 Systematic Uncertainties of the $Z/\gamma^* \rightarrow \tau\tau$ Embedded Sample

An important element of the embedding method is the subtraction of the calorimeter cells associated with the muons in the original $Z \rightarrow \mu\mu$ event and their substitution with those from the simulated τ lepton decays. To make a conservative estimate of the systematic uncertainty on this procedure, the energy of the subtracted cells is scaled up or down by 30%. The analysis is repeated with those modified samples and the relative uncertainty is referred as "EMB_MFS". This

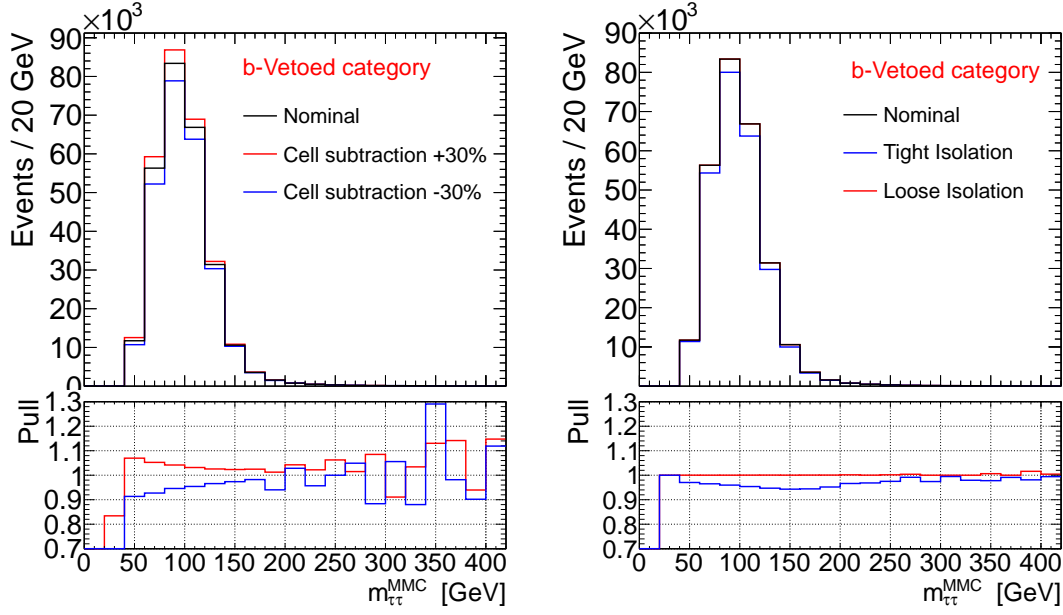


Figure 1.13: Impact of EMB_MFS (left) and EMB_ISO (right) systematic uncertainties on the $m_{\tau\tau}^{MMC}$ mass distribution for in the embedded sample. Significant impact is observed only in the b-vetoed event category.

uncertainty affects mainly the shape of the $m_{\tau\tau}^{MMC}$ mass distribution, shown in Figure 1.13.

In the sample of $Z \rightarrow \mu\mu$ candidates used for the embedding, only a loose requirement on the muon track isolation is applied. A different muon isolation requirement may affect the selected sample by modifying the topology of the event, changing the contamination with other processes or the activity in the calorimeter. To estimate the importance of these effects in the embedded sample, the muon isolation criteria used in the original $Z \rightarrow \mu\mu$ sample are tightened, while an even looser selection would have a rather small impact due to isolation requirements at the trigger level. The resulting uncertainty, referred to as "EMB_ISO", affects both the event yield and the shape of the $m_{\tau\tau}^{MMC}$ mass distribution in the embedded sample, as shown in Figure 1.13.

Finally, because the normalization of the embedded sample is determined from

Selection	R_{QCD}	R_{QCD}^{AB}	R_{QCD}^{iso}
common selection	1.929 ± 0.004	2.12 ± 0.17	2.22 ± 0.16
No b-tagged jets	1.965 ± 0.005	2.10 ± 0.16	2.22 ± 0.16
Exactly one b-tagged jet	1.78 ± 0.02	1.9 ± 0.9	2.0 ± 0.8

Table 1.13: Comparison between R_{QCD} , R_{QCD}^{AB} and R_{QCD}^{iso} after the common selection stage and after requiring or vetoing the presence of b-tagged jets. Only the statistical uncertainty is reported here. The value of R_{QCD}^{iso} is reported for the lepton isolation threshold which is twice the nominal value, while for R_{QCD}^{AB} and R_{QCD} the nominal values are reported.

the simulated ALPGEN sample, the uncertainties related to the cross section and to luminosity are assigned. In addition all detector-related systematic uncertainties relevant to the decay products of the simulated τ lepton decay are propagated to the embedded sample.

1.4.4 QCD Multi-Jet Systematic Uncertainties

The QCD multi-jet background is estimated via the ABCD method, as described in Section 1.3.2. This technique relies strongly on the assumption that the lepton isolation variables are uncorrelated to the relative charge of the two leptons. Systematic uncertainties are assigned to take into account possible deviations from this assumption. First the correlation between the ratio R_{QCD} and the lepton isolation criteria is considered, then the result is compared with an auxiliary measurement.

Figure 1.14 shows the R_{QCD} factor, i.e. the ratio between the QCD yields in data samples C and D, as a function of a sliding lepton isolation threshold relative to the nominal analysis selection (red points). As described previously, the expected contamination of non-QCD background processes is subtracted from the data in samples C and D. To estimate the uncertainty on the value of R_{QCD} an additional transfer factor is defined: $R_{QCD}^{iso} = N_{\hat{A}}/N_{\hat{B}}$, where \hat{A} and \hat{B} are semi-isolated OS and SS samples defined by requiring the lepton isolation to be larger

than the nominal one, but smaller than a given sliding threshold value (defined by the X -axis of the plot). Also here the non-QCD contributions are subtracted from the data yields. The semi-isolated samples \hat{A} and \hat{B} are chosen given the high contamination with non-QCD background processes and with possible signal in data samples A and B. Figure 1.14 shows R_{QCD}^{iso} as a function of the relative lepton isolation threshold (black points). The difference between R_{QCD} and R_{QCD}^{iso} in the vicinity of the nominal isolation threshold is then assigned as a systematic uncertainty on R_{QCD} . For the lepton isolation threshold which is twice the nominal value, a systematic uncertainty of 15% is found. The result shown in Figure 1.14 are obtained after common selection. Similar results after the full analysis selection in the two event categories are shown in Appendix B.

As a test of the result described above an additional measurement is performed. The R_{QCD}^{AB} is calculated as the ratio between the estimated QCD multi-jet contributions in samples A and B instead of C and D. The non-QCD contributions are subtracted from data. Due to the large contribution of this non-QCD background, along with small numbers of observed events and possible signal contamination, this measurement is only used for cross check. Table 1.13 shows a comparison between R_{QCD} , R_{QCD}^{iso} and R_{QCD}^{AB} after the common selection stage and after requiring or vetoing the presence of b-tagged jets, at these selection stages the signal contamination is negligible. Good agreement is seen between the results of these methods.

The shape of the $m_{\tau\tau}^{MMC}$ mass distribution differs between the OS and SS in anti-isolated samples (C and D) as shown in Figure 1.15. The size of this effect is within the above R_{QCD} uncertainty for the relevant mass range of the QCD multi-jet background (QCD multi-jet background contribution is negligible for $m_{\tau\tau}^{MMC} > 150$ GeV) and hence no correction factor is applied to the mass shape of sample B. It is assumed, however, that there could be the same shape difference in the isolated samples and thus a shape uncertainty is assigned to the mass distribution in sample B to account for this deviation. Further shape uncertainties due to non-QCD background subtraction are found to be negligible. The uncertainty due to the use of an isolation requirement at the trigger level is

discussed in Appendix A and is found to be negligible.

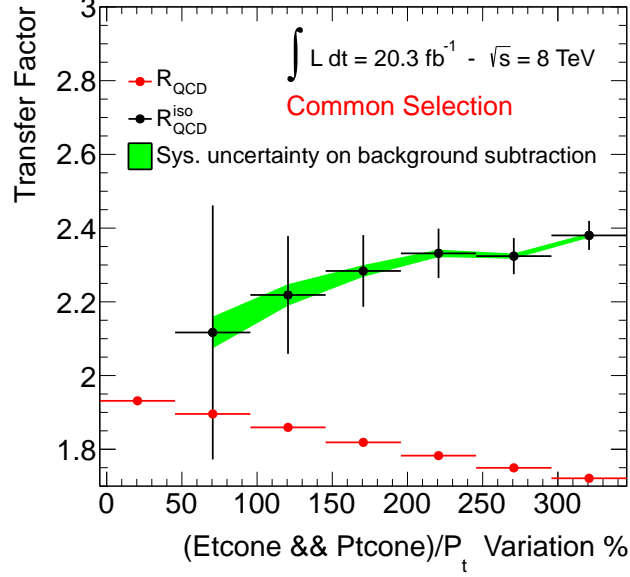


Figure 1.14: Transfer factors R_{QCD} and R_{QCD}^{iso} (see text) as a function of the sliding lepton isolation thresholds. The thresholds are varied in percentages relative to the nominal lepton isolation threshold (value of zero on the plot). The common selection are applied.

1.5 Results

1.5.1 Statistical Procedure

The statistical interpretation of data in the presented search is based on profiled likelihood ratio test statistic used for the Higgs boson searches [140]. The statistical procedures described in the following are implemented in the software packages described in [141–143].

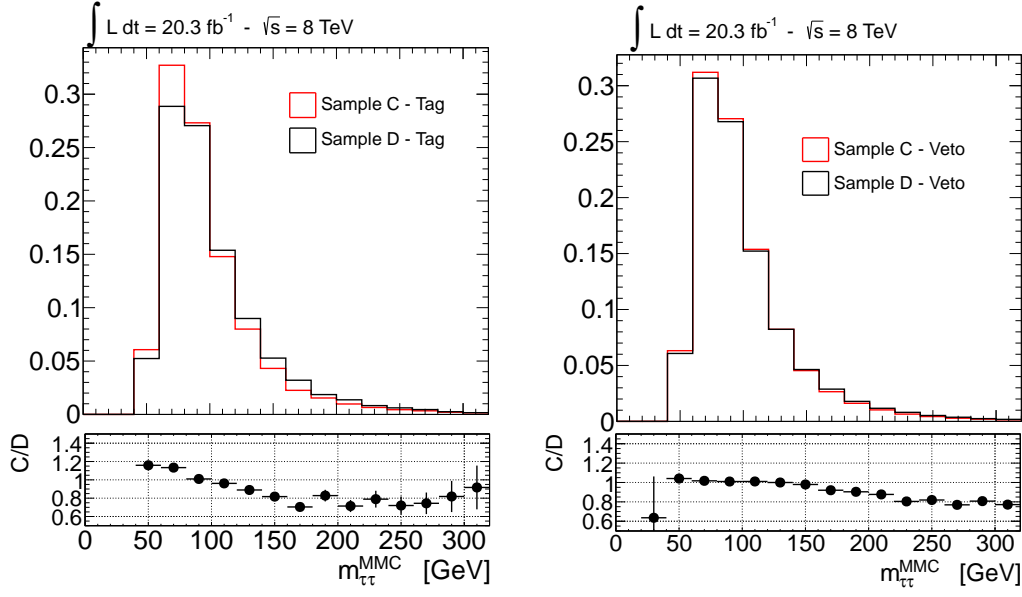


Figure 1.15: Differences in the shape of the invariant $m_{\tau\tau}^{MMC}$ mass distribution in data samples C and D shown separately for the b-taged and b-vetoed event categories. The data samples C and D are normalised to the same number of events.

The Likelihood Function

The statistical interpretation of data is performed by means of testing the compatibility of the *background only* and the *signal-plus-background* hypotheses with the observed data. The main ingredient of the hypothesis *test statistic*, defined later on in this section, is a binned likelihood function for the data set, \mathcal{D} :

$$\mathcal{L}(\mathcal{D} \mid \mu, \boldsymbol{\theta}) = \text{Pois}(\mathcal{D} \mid \mu \cdot s(\boldsymbol{\theta}) + b(\boldsymbol{\theta})) \cdot \prod_{j,i} \mathcal{G}(\theta_j^{sys} \mid 0, 1) \cdot \Gamma(\theta_i^{stat} \mid \beta_i) \quad (1.4)$$

describing how likely is a certain hypothesis given the observation of the data set \mathcal{D} . The signal strength modifier μ allows for reproducing a continuous set of signal hypotheses with different cross-section. The value of $\mu = 0$ corresponds to the background-only hypothesis. The vector $\boldsymbol{\theta}$ represents the set of *nuisance* parameters related to the systematic (θ_j^{sys}) and to the statistical (θ_i^{stat}) uncertainties of the background and signal predictions. The functions $s(\boldsymbol{\theta})$ and $b(\boldsymbol{\theta})$ represent

the expected signal and background distribution respectively, these are binned histograms of the invariant $m_{\tau\tau}^{MMC}$ mass distribution. The function $\mathcal{G}(\theta_j^{sys} | 0, 1)$ is the Gaussian³ probability density function (p.d.f.) for the nuisance parameter θ_j^{sys} , which is assumed to be distributed with mean = 0 and $\sigma = 1$. The impact of the corresponding systematic uncertainty on the signal and backgrounds yields and on the shape of the $m_{\tau\tau}^{MMC}$ invariant mass distribution is evaluated separately as described in Section 1.4. The function $\Gamma(\theta_i^{stat} | \beta_i)$ is an extended gamma function⁴ describing the p.d.f. for the nuisance parameter θ_i^{stat} related to the statistical uncertainty β_i , for the bin i of the considered histogram. Each value of the nuisance parameter set $\boldsymbol{\theta}$ is associated with a variation of the predicted signal and background event yields with respect to the nominal prediction. The Poisson distribution in equation (1.4) is a binned p.d.f. and stands for a product of Poisson probabilities to observe n_i events in the bin i of the $m_{\tau\tau}^{MMC}$ mass distribution histogram:

$$\text{Pois}(\mathcal{D} | \mu \cdot s(\boldsymbol{\theta}) + b(\boldsymbol{\theta})) = \prod_i \frac{(\mu s_i(\boldsymbol{\theta}) + b_i(\boldsymbol{\theta}))^{n_i}}{n_i!} e^{-\mu s_i(\boldsymbol{\theta}) - b_i(\boldsymbol{\theta})}$$

The $m_{\tau\tau}^{MMC}$ mass distributions in the b-tagged and b-vetoed category are analysed separately. The actual implementation in the likelihood function of the ABCD method follows that suggested in [134] and it is described in more detail in Appendix C.

Statistical Combination of Results From Two Event Categories

Complementary event categories in one search channel, like the b-tagged and b-vetoed event categories, can be combined in order to increase the sensitivity to the signal. If there are no events entering both categories, as is the case for the presented analysis, the statistical combination is the product of the likelihood functions for the individual categories. For the combination, the convention described

³Evaluation of systematic uncertainties is obtained from auxiliary measurements. From Bayes theorem, assuming a flat prior and a Gaussian distribution for the measured parameter a Gaussian posterior is obtained.

⁴The posterior of a Poisson distribution assuming a flat prior is a gamma function

in [140] is used to take into account the correlation between different sources of uncertainties. Uncertainties are considered either as fully correlated, which means that the same nuisance parameter is describing the given systematic effect in both categories, or fully uncorrelated, in which case different nuisance parameter are employed in the two categories. Partially correlated uncertainties are either split into component which are fully uncorrelated or they are defined as to either fully correlated or uncorrelated, depending on which assumption is the most conservative.

The Test Statistic and the Exclusion Limits

To compute the compatibility of the data with a given hypothesis a test statistic is defined based on the *profiled likelihood ratio* [144]:

$$\tilde{q}_\mu = -2 \ln \frac{\mathcal{L}(\mathcal{D} \mid \mu, \hat{\boldsymbol{\theta}}_\mu)}{\mathcal{L}(\mathcal{D} \mid \hat{\mu}, \hat{\boldsymbol{\theta}})} \quad \text{with the constraint} \quad 0 \leq \hat{\mu} \leq \mu. \quad (1.5)$$

where \mathcal{L} is the likelihood function defined in equation (1.4), $\hat{\mu}$ and $\hat{\boldsymbol{\theta}}$ are the global maximum likelihood estimators for μ and $\boldsymbol{\theta}$ given the data, whereas $\hat{\boldsymbol{\theta}}_\mu$ is the maximum likelihood estimator of $\boldsymbol{\theta}$ given the data but with a signal strength fixed to the value of μ . \tilde{q}_μ is increasing with increasing disagreement between data and the given μ hypothesis. Based on this, the procedure for setting upper exclusion limits on the signal cross-section is defined as follows:

1. The probability density function of \tilde{q}_μ is determined under the background-only (H_0) and the signal-plus-background (H_μ) hypotheses for any given value of μ . Since the determination of these distributions by means of pseudo-data demands large computing resources, asymptotic approximation formulas described in [144] are employed.
2. Once the p.d.f. for the background-only and signal-plus-background hypothesis are obtained, it is possible to define for a given dataset two probability values (p-values) for any given value of μ . These are the probabilities to obtain data less compatible with the considered hypothesis than the actual

observation:

$$p_{s+b} = P(\tilde{q}_\mu > \tilde{q}_\mu^{observed} \mid H_\mu)$$

$$p_b = P(\tilde{q}_\mu > \tilde{q}_\mu^{observed} \mid H_0)$$

The ratio of this two probabilities defines the quantity $CL_s = p_{s+b}/p_b$ [145, 146].

3. If for a given μ the CL_s value of $CL_s \leq \alpha$ is obtained, the signal-plus-background hypothesis (with the corresponding μ value) is considered to be excluded at a $(1 - \alpha)$ CL_s confidence level. The 95% confidence level upper limit on μ , denoted as $\mu^{95\%}$, is defined as the smallest value of μ for which the CL_s is no longer greater than 0.05.

By construction, rejecting all values of $\mu > \mu^{95\%}$, the signal-plus-background hypothesis will be rejected when it is true at most 5% of the time. The CL_s prescription is a conservative approach protecting the signal exclusion upper limit from downward fluctuation of the data. The expected median exclusion upper-limit and its error are evaluated with the procedure described above under the background-only hypothesis. The obtained results have been cross-checked using generated pseudo-data instead of the asymptotic approximation for the determination of the \tilde{q}_μ probability density functions.

1.5.2 Exclusion Limits on the Signal Production

The statistical procedure described in section 1.5.1 is the general one used for the SM Higgs boson where only the Higgs boson mass determines the signal properties. For the MSSM further complication arises: there are three neutral Higgs bosons contributing to the total signal yield, in a particular scenario the masses and cross section are defined by two parameter $\tan \beta$ and m_A . Thus, the previously described procedure has to be repeated for each point in the $\tan \beta - m_A$ plane. For the m_h^{mod} scenario exclusion limits at 95% CLs confidence level are derived on the cross section for the neutral MSSM Higgs bosons ($A/h/H$) production via gluon fusion and in association with b-quarks, the considered Higgs bosons

decay is $A/H/h \rightarrow \tau\tau \rightarrow \mu e + 4\nu$. A scan has been performed over for 15 $\tan\beta$ values ranging⁵ from $\tan\beta = 5$ to $\tan\beta = 60$. A point in the $\tan\beta - m_A$ plane is excluded if $\mu^{95} \leq 1$ for that point. A linear interpolation is used to determine the excluded $\tan\beta$ for a given m_A . The procedure is repeated for a set of 12 CP-odd Higgs boson masses values m_A ranging from 90 GeV to 300 GeV⁶. The expected and observed event yields are compared in bins of the $m_{\tau\tau}^{MMC}$ mass distribution. The bin sizes are chosen such that the number of events per bin is high enough to justify the use of the asymptotic approximation. Table 1.14 compares the expected and the observed event yields in the two event categories at the final stage of the event selection. Additionally, Figure 1.16 shows the corresponding $m_{\tau\tau}^{MMC}$ mass distributions.

The resulting exclusion limit on the MSSM $m_A - \tan\beta$ parameter space are interpreted within the m_h^{mod} benchmark scenario and shown in Figure 1.17. The expected and observed exclusion limits at 95% CL_s confidence-level are shown as dashed and solid black lines respectively. The green and yellow bands correspond to the 1σ and 2σ error bands on the expected exclusion limit. The analysis is sensitive to the MSSM Higgs boson production for $\tan\beta \geq 13$ and the mass range $90 < m_A < 200$ GeV. The observed limit is

The outcome of the search is also interpreted in a model-independent way, by setting the limits on the production cross-section of a scalar boson produced in the $pp \rightarrow gg \rightarrow \phi$ or $pp \rightarrow b\bar{b}\phi$ mode and decaying in a di-tau pair. The corresponding expected and observed 95% CL_s confidence-level limits are shown in Figure 1.18. The limits in the production in association with b-quarks and via gluon fusion are shown separately. More information on the limit setting procedure and its validation can be found in Appendix C.

⁵ The set of $\tan\beta$ values used is 5, 8, 10, 13, 16, 20, 23, 26, 30, 35, 40, 45, 50, 55, 60

⁶ The set of m_A values used is: 90, 100, 110, 120, 125, 130, 140, 150, 170, 200, 250 and 300 GeV

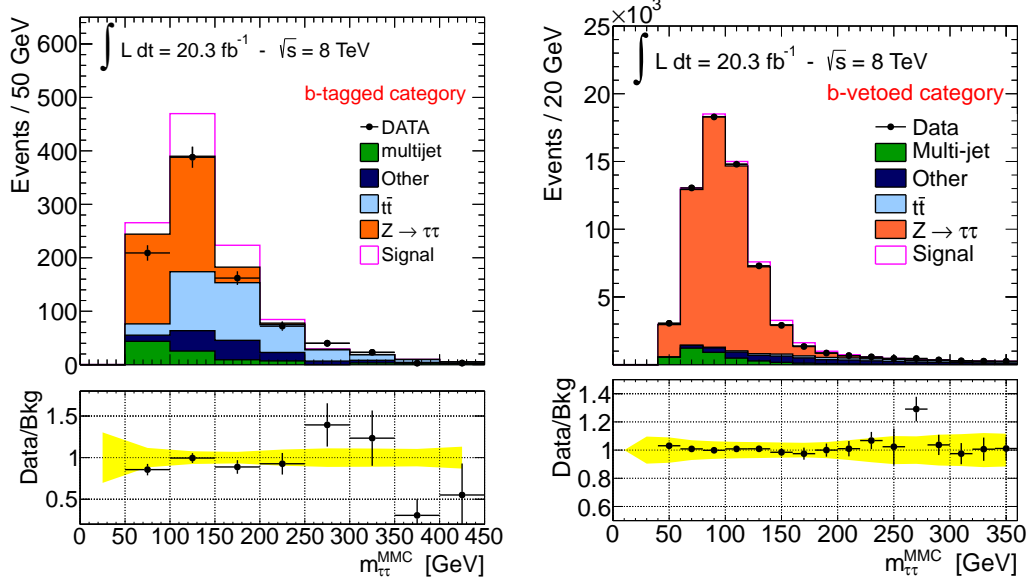


Figure 1.16: Observed and expected distribution of the $m_{\tau\tau}^{MMC}$ mass for (left) the b-tagged event category and (right) the b-vetoed event category after the full event selections. The prediction of the background model is compared to data. The contribution of the $Z/\gamma^* \rightarrow \tau\tau$ and QCD multi-jet background processes is measured in dedicated signal-depleted control data samples, the prediction for all the other background processes is obtained from simulation. The notation “Other” stands for the electroweak processes $W \rightarrow \ell\nu$, $Z \rightarrow \ell\ell$, diboson and single top quark production. The prediction for the signal is evaluated considering the production of the three neutral MSSM Higgs bosons in association with b-quarks and via the gluon fusion processes in the m_H^{mod} scenario for values of $m_A = 150$ GeV and $\tan\beta = 20$. The yellow band represents the total systematic uncertainty for the background model prediction.

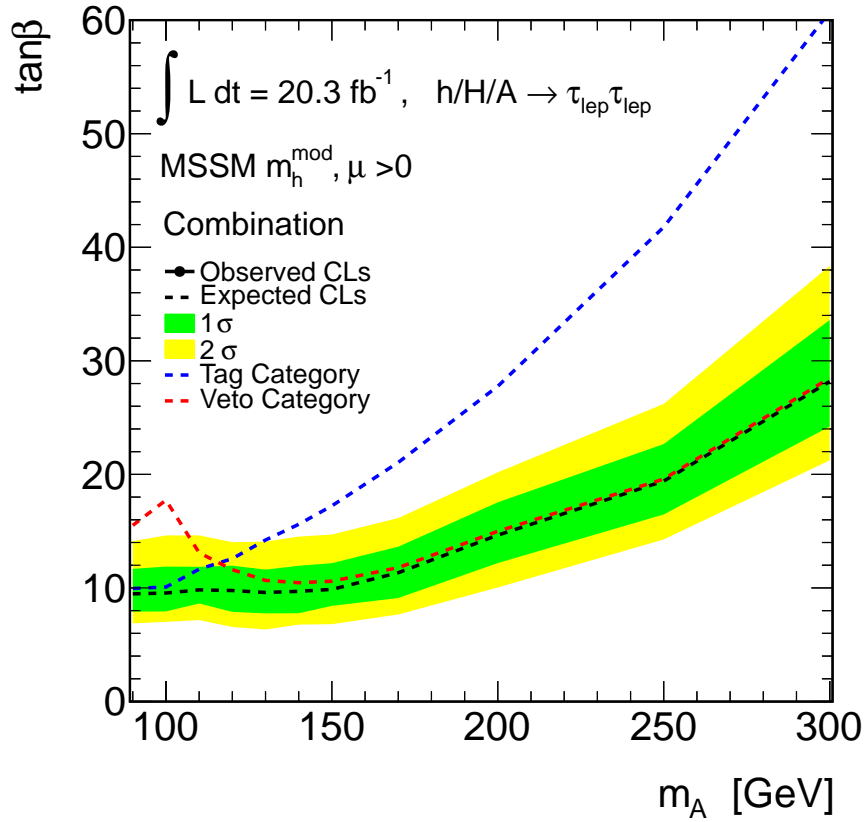


Figure 1.17: Expected and observed exclusion limits at the 95% CL_s confidence-level for MSSM Higgs bosons production interpreted in the $m_A - \tan \beta$ parameter space of the m_h^{mod} scenario. Combined result of the b-tagged and b-vetoed category is shown.

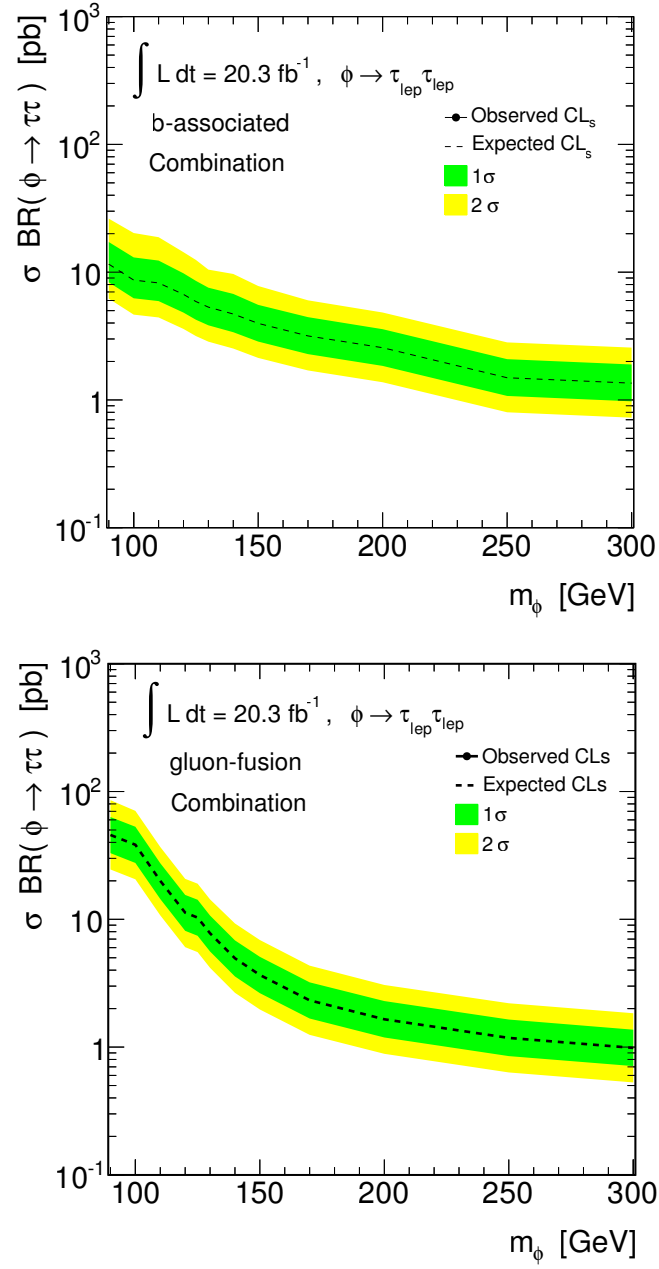


Figure 1.18: Limits on the production of a scalar particle decaying to a di-tau pair and produced in association with b quarks (top) or via gluon-gluon fusion (bottom).

Sample	b-tag category			b-veto category		
	N(event)	Stat.	Syst.	N(event)	Stat.	Syst.
$Z/\gamma^* \rightarrow \tau\tau$	418	± 6	$^{+27}_{-27}$	54680	± 60	$^{+3500}_{-3500}$
$t\bar{t}$	330	± 10	$^{+37}_{-35}$	2159	± 25	$^{+280}_{-300}$
Multijet	101	± 15	$^{+15}_{-15}$	3930	± 330	$^{+590}_{-590}$
Other	114	± 9	$^{+12}_{-12}$	4450	± 110	$^{+250}_{-250}$
Total	963	± 21	$^{+50}_{-50}$	65220	± 360	$^{+3600}_{-3600}$
Signal	144	± 7	$^{+24}_{-33}$	2028	± 27	$^{+150}_{-100}$
Data	-	-	-	-	-	-

Table 1.14: Expected and observed number event yields in the b-tagged and b-vetoed event category after the full event selections. The various background and signal expected event yields are normalized to the integrated luminosity of the data sample (20.3 fb^{-1}). The notation “Other” stands for the electroweak processes $W \rightarrow \ell\nu$, $Z \rightarrow \ell\ell$, diboson and single top quark production. $Z/\gamma^* \rightarrow \tau\tau$ has been estimated using the embedding technique. The uncertainties quoted include the statistical uncertainty (first number) and the systematic uncertainties (second number). For the prediction of the MSSM Higgs bosons signal yield, $m_A = 150 \text{ GeV}$ and $\tan\beta = 20$ is assumed in the m_h^{mod} scenario.

Bibliography

- [1] G. Altarelli, “*Collider Physics within the Standard Model: a Primer*,” arXiv:1303.2842 .
- [2] S. P. Martin, “*A Supersymmetry primer*,” In *Kane, G.L. (ed.): Perspectives on supersymmetry II* 1-153 [hep-ph/9709356].
- [3] A. Djouadi, *The Anatomy of Electroweak Symmetry Breaking Tome II: The Higgs Bosons in the Minimal Supersymmetric Model*, Phys. Rep. 459 (2008) 1.
- [4] S. Heinemeyer *et al.* [LHC Higgs Cross Section Working Group Collaboration], “Handbook of LHC Higgs Cross Sections: 3. Higgs Properties,” arXiv:1307.1347
- [5] S. Dittmaier *et al.* [LHC Higgs Cross Section Working Group Collaboration], “*Handbook of LHC Higgs Cross Sections: 1. Inclusive Observables*,” arXiv:1101.0593
- [6] Michael E. Peskin, Dan V. Schroeder, *An Introduction To Quantum Field Theory*, Westview Press, 1995.
- [7] S. L. Glashow, Partial Symmetries of Weak Interactions, Nuc. Phys. 22 (1961) 579.
- [8] A. Salam, Weak and Electromagnetic Interactions, Conf. Proc. C 680519 (1968) 367. Originally printed in Svartholm: Elementary Particle Theory, proceedings of the Nobel Symposium held 1968 at Lerum, Sweden.
- [9] S. Weinberg, A Model of Leptons, Phys. Rev. Lett. 19 (1967) 1264.

- [10] H. Fritsch, M. Gell-Mann, and H. Leutwyler, Advantages of the Color Octet Gluon Picture, *Phys. Lett. B* **47** (1973) 365.
- [11] F. Englert and R. Brout, *Broken Symmetry and the Mass of Gauge Vector Mesons*, *Phys. Rev. Lett.* **13** (1964) 321.
- [12] P. W. Higgs, *Broken symmetries, massless particles and gauge fields*, *Phys. Lett.* **12** (1964) 132.
- [13] P. W. Higgs, *Broken Symmetries and the Masses of Gauge Bosons*, *Phys. Rev. Lett.* **13** (1964) 508.
- [14] P. W. Higgs, *Spontaneous Symmetry Breakdown without Massless Bosons*, *Phys. Rev.* **145** (1966) 1156.
- [15] T. W. B. Kibble, Symmetry Breaking in NonAbelian Gauge Theories, *Phys. Rev.* **155** (1967) 1554.
- [16] The ATLAS Collaboration, *Observation of a new particle in the search for the Standard Model Higgs boson with the ATLAS detector at the LHC*, *Physics Letters B* **716** (2012) 1–29.
- [17] The CMS Collaboration, *Observation of a new boson at a mass of 125 GeV with the CMS experiment at the LHC*, *Physics Letters B* **716** (2012) 30–61.
- [18] W. Hollik, “*Electroweak theory*,” hep-ph/9602380.
- [19] The Review of Particle Physics, J. Beringer et al. (Particle Data Group), *Phys. Rev. D* **86**, 010001 (2012) and 2013 partial update for the 2014 edition.
- [20] The ALEPH, CDF, D0, DELPHI, L3, OPAL and SLD Collaborations, the LEP Electroweak Working Group, Tevatron Working Group and SLD Electroweak and Heavy Flavour Working Groups, *Precision Electroweak Measurements and Constraints on the Standard Model*, arXiv:1012.2367. Updated for 2012 winter conferences, March 2012.

- [21] The Gfitter Group, M. Baak, et al., Updated Status of the Global Electroweak Fit And constraints on New Physics, Eur. Phys. J. C 72 (2012) 2003. Updated for 2012 winter conferences, March 2012, <http://gfitter.desy.de>.
- [22] G.W. Bennett et al., Phys. Rev. Lett. 89, 101804 (2002); Erratum ibid. Phys. Rev. Lett. 89, 129903 (2002); G.W. Bennett et al., Phys. Rev. Lett. 92, 161802 (2004); G.W. Bennett et al., Phys. Rev. D73, 072003 (2006).
- [23] B. Bhattacharjee, S. S. Biswal and D. Ghosh, *Top quark forward-backward asymmetry at Tevatron and its implications at the LHC*, Phys. Rev. D **83** (2011) 091501 [arXiv:1102.0545 [hep-ph]].
- [24] M. Veltman, Acta. Phys. Pol. B8 (1977) 475.
- [25] S. Weinberg, Gauge Hierarchies, Phys. Lett. B 82 (1979) 387.
- [26] M. Veltman, The InfraredUltraviolet Connection, Acta Phys. Polon. B 12 (1981) 437.
- [27] C. Smith and G. Ross, The Real Gauge Hierarchy Problem, Phys. Lett. B 105 (1981) 38.
- [28] F. Zwicky, Spectral Displacement of Extra Galactic Nebulae, Helv. Phys. Acta 6 (1933) 110.
- [29] E. W. Kolb and M. S. Turner, The Early Universe, Front. Phys. 69 (1990) 1.
- [30] The WMAP Collaboration, D. N. Spergel et al., First Year Wilkinson Microwave Anisotropy Probe (wmap) Observations: Determination of Cosmological Parameters, Astrophys. J. Suppl. 148 (2003) 175.
- [31] H. M. Georgi and S. L. Glashow, Unity of All ElementaryParticle Forces, Phys. Rev. Lett. 32 (1974) 438.
- [32] J. C. Pati and A. Salam, Lepton Number as the Fourth Color, Phys. Rev. D 10 (1974) 275.

- [33] P. Fayet, Phys. Lett. B 64, 159 (1976).
- [34] P. Fayet, Phys. Lett. B 69, 489 (1977), Phys. Lett. B 84, 416 (1979).
- [35] G.R. Farrar and P. Fayet, Phys. Lett. B 76, 575 (1978).
- [36] S. Martin, in Perspectives on Supersymmetry, Ed. G.L. Kane, World Scientific, Singapore, 1998, hep-ph/9709356.
- [37] For reviews on the MSSM, see: P. Fayet and S. Ferrara, Phys. Rep. 32 (1977) 249; H.P. Nilles, Phys. Rep. 110 (1984) 1; R. Barbieri, Riv. Nuovo Cim. 11N4 (1988) 1; R. Arnowitt and Pran Nath, Report CTP-TAMU-52-93; J. Bagger, Lectures at TASI-95, hep-ph/9604232.
- [38] H. E. Haber and G. Kane, Phys. Rep. 117 (1985) 75.
- [39] M. Drees and S. Martin, CLTP Report (1995) and hep-ph/9504324.
- [40] D.J.H. Chung, L.L. Everett, G.L. Kane, S.F. King, J. Lykken and L.T. Wang, Phys. Rept. 407 (2005) 1.
- [41] M. Drees, R.M. Godbole and P. Roy, Theory and Phenomenology of Sparticles, World Scientific, Spring 2004.
- [42] L. Girardello and M.T. Grisaru, Nucl. Phys. B194 (1982) 65.
- [43] Y. Okada, M. Yamaguchi and T. Yanagida, Prog. Theor. Phys. 85 (1991) 1; *ibid.* Phys. Lett. B262 (1991) 54; J.R. Ellis, G. Ridolfi and F. Zwirner, Phys. Lett. B257 (1991) 83; *ibid.* Phys. Lett. B262 (1991) 477; H.E. Haber and R. Hempfling, Phys. Rev. Lett. 66 (1991) 1815.
- [44] A. Djouadi and S. RosiersLees (conv.) et al., Summary Report of the MSSM Working Group for the GDRSupersym trie, hep-ph/9901246.
- [45] K. Inoue, A. Komatsu and S. Takeshita, Prog. Theor. Phys 68 (1982) 927; (E) *ibid.* 70 (1983) 330.

- [46] E. Witten, Nucl. Phys. B188 (1981) 513; *ibid* Nucl. Phys. B202 (1982) 253; N. Sakai, Z. Phys. C11 (1981) 153; S. Dimopoulos and H. Georgi, Nucl. Phys. B193 (1981) 150; R.K. Kaul and P. Majumdar, Nucl. Phys. B199 (1982) 36.
- [47] J.F. Donoghue and L.F. Li, Phys. Rev. 19 (1979) 945.
- [48] J.F. Gunion and H.E. Haber, Nucl. Phys. B278 (1986) 449.
- [49] J.F. Gunion and H.E. Haber, Nucl. Phys. B272 (1986) 1; (E) hep-ph/9301205.
- [50] M. Frank et al., The Higgs Boson Masses and Mixings of the Complex MSSM in the FeynmanDiagrammatic Approach, JHEP 0702 (2007) 47.
- [51] M. Carena, S. Heinemeyer, C. E. M. Wagner, and G. Weiglein, *Suggestions for benchmark scenarios for MSSM Higgs boson searches at hadron colliders*, Eur. Phys. J. **C26** (2003) 601–607, hep-ph/0202167.
- [52] S. Heinemeyer, O. Stal, and G. Weiglein, *Interpreting the LHC Higgs Search Results in the MSSM*, Phys. Lett. B 710 (2012) 201206, arXiv:1112.3026.
- [53] The ATLAS Collaboration, *Constraints on New Phenomena via Higgs Boson Coupling Measurements with the ATLAS Detector*. ATLAS-CONF-2014-010.
- [54] L. Maiani, A. Polosa, and V. Riquer, Bounds to the Higgs Sector Masses in Minimal Supersymmetry from LHC Data, arXiv:1305.2172.
- [55] A. Djouadi, L. Maiani, G. Moreau, A. Polosa, J. Quevillon, et al., The post-Higgs MSSM scenario: Habemus MSSM?, arXiv:1307.5205.
- [56] L. Evans and P. Bryant, *LHC Machine*, JINST **3** (2008) S08001.
- [57] The ATLAS Collaboration, G. Aad et al., *The ATLAS Experiment at the CERN Large Hadron Collider*, JINST **3** (2008) S08003.
- [58] J. Haffner, *The CERN accelerator complex*, OPEN-PHO-ACCEL-2013-056.
- [59] CMS Collaboration, CMS technical proposal, CERN-LHCC-94-38.

- [60] LHCb Collaboration, LHCb technical proposal, CERN-LHCC-98-004.
- [61] ALICE Collaboration, ALICE: Technical proposal for a large ion collider experiment at the CERN LHC, CERN-LHCC-95-71, CERN, 1995,
- [62] G. S. Guralnik, C.R. Hagen and T. W. B. Kibble Phys.Rev.Lett. **13** (1964) 585.
- [63] The ATLAS Collaboration, *Luminosity Determination in pp Collisions at $\sqrt{s} = 7$ TeV using the ATLAS Detector in 2011*, ATLAS-CONF-2011-116.
- [64] ALEPH, DELPHI, L3 and OPAL Collaboration, *Search for neutral MSSM Higgs bosons at LEP*, Eur. Phys. J. **C47** (2006) 547.
- [65] *Combined CDF and D0 upper limits on MSSM Higgs boson production in tau-tau final states with up to 2.2 fb^{-1} of data*, arXiv:1003.3363 [hep-ex].
- [66] The CMS Collaboration, S. Chatrchyan et al., arXiv:1104.1619 [hep-ex] [hep-ex].
- [67] The ATLAS Collaboration, *Search for the neutral Higgs bosons of the Minimal Supersymmetric Standard Model in pp collisions at $\sqrt{s} = 7$ TeV with the ATLAS detector*, arXiv:1211.6956 [hep-ex].
- [68] S. Heinemeyer, O. Stål and G. Weiglein, *Interpreting the LHC Higgs search results in the MSSM*, Phys.Lett. **B710** (2012) 201–206, arXiv:1112.3026 [hep-ph].
- [69] A. Arbey, M. Battaglia, A. Djouadi and F. Mahmoudi, *The Higgs sector of the phenomenological MSSM in the light of the Higgs boson discovery*, JHEP **1209** (2012) 107, arXiv:1207.1348 [hep-ph].
- [70] M. L. Mangano et al., *ALPGEN, a generator for hard multiparton processes in hadronic collisions*, JHEP **07** (2003) 001.

- [71] J. Alwall et al., *Comparative study of various algorithms for the merging of parton showers and matrix elements in hadronic collisions*, Eur. Phys. J. **C53** (2008) 473, [arXiv:0706.2569](#).
- [72] S. Frixione and B. R. Webber, *Matching NLO QCD computations and parton shower simulations*, JHEP **06** (2002) 029, [hep-ph/0204244](#).
- [73] B. P. Kersevan and E. Richter-Was, *The Monte Carlo Event Generator AcerMC 2.0 with Interfaces to PYTHIA 6.2 and HERWIG 6.5*, [arXiv:0405247v1 \[hep-ph\]](#).
- [74] G. Corcella et al., *HERWIG 6: an event generator for hadron emission reactions with interfering gluons (including supersymmetric processes)*, JHEP **01** (2001) 010.
- [75] J. M. Butterworth, J. R. Forshaw, and M. H. Seymour, *Multiparton Interactions in Photoproduction at HERA*, Z. Phys. **C72** (1996) 637.
- [76] T. Binoth, M. Ciccolini, N. Kauer, and M. Kramer, *Gluon-induced W-boson pair production at the LHC*, JHEP **12** (2006) 046.
- [77] A. S. et al., *Higgs boson production in gluon fusion*, JHEP **02** (2009) 029.
- [78] T. Gleisberg et al., *Event generation with SHERPA 1.1*, JHEP **02** (2009) 007.
- [79] J. Pumplin, D. R. Stump, J. Huston, H. L. Lai, P. M. Nadolsky and W. K. Tung, “New generation of parton distributions with uncertainties from global QCD analysis,” JHEP **0207** (2002) 012 [[hep-ph/0201195](#)].
- [80] H. -L. Lai, M. Guzzi, J. Huston, Z. Li, P. M. Nadolsky, J. Pumplin and C. -P. Yuan, “New parton distributions for collider physics,” Phys. Rev. D **82** (2010) 074024 [[arXiv:1007.2241 \[hep-ph\]](#)].
- [81] The ATLAS Collaboration, *ATLAS Monte Carlo Tunes for MC09*, ATL-PHYS-PUB-2010-002.

- [82] S. Jadach, J. H. Kuhn and Z. Was, *TAUOLA - a library of Monte Carlo programs to simulate decays of polarized τ leptons*, Comput. Phys. Commun. **64** (1990) 275.
- [83] E. Barberio, B. V. Eijk and Z. Was, *Photos - a universal Monte Carlo for QED radiative corrections in decays*, Comput. Phys. Commun. **66** (1991) 115.
- [84] The GEANT4 Collaboration, S. Agostinelli et al., *GEANT4 - a simulation toolkit*, Nucl. Instrum. Meth. **A506** (2003) 250.
- [85] The ATLAS Collaboration, G. Aad et al., *The ATLAS Simulation Infrastructure*, ATLAS-SOFT-2010-01-004, submitted to Eur. Phys. J. C., arXiv:1005.4568.
- [86] The ATLAS Collaboration, *Estimation of $Z/\gamma^* \rightarrow \tau\tau$ Background in VBF $H \rightarrow \tau\tau$ Searches from $Z \rightarrow \mu\mu$ Data using an Embedding Technique*, ATL-PHYS-INT-2009-109.
- [87] The ATLAS Collaboration, *Search for the Standard Model Higgs boson in the $H \rightarrow \tau\tau$ decay mode with 4.7 fb of ATLAS detector*, Tech. Rep. ATLAS-CONF-2012-014, CERN, Geneva, Mar, 2012.
- [88] The ATLAS Collaboration, *Search for the Standard Model Higgs boson $H \rightarrow \tau\tau$ decays with the ATLAS detector*, ATL-COM-PHYS-2013-722.
- [89] T. S. et al., *Z physics at LEP 1*, CERN 89-08 **3** (1989) 143.
- [90] The ATLAS Collaboration, *Inner Detector: Technical Design Report*, CERN/LHCC/97-016/017 (1997).
- [91] The ATLAS Collaboration, G. Aad et al., *The ATLAS Experiment at the CERN Large Hardon Collider*, 2008 JINST **3** S08003.
- [92] A. Bazan, T. Bouedo, P. Ghez, M. Marino and C. Tull, “The Athena data dictionary and description language,” eConf C **0303241** (2003) MOJT010 [cs/0305049 [cs-se]].

- [93] The ATLAS Collaboration, *Expected Performance of the ATLAS Experiment - Detector, Trigger and Physics*, CERN-OPEN-2008-020, [arXiv:0901.0512](#).
- [94] T. Cornelissen et al., Concepts, Design and Implementation of the ATLAS New Tracking, ATLAS Note ATL-SOFT-PUB-2007-007 (2007).
- [95] Kalman, R. E. (1960). "*A New Approach to Linear Filtering and Prediction Problems*". Journal of Basic Engineering 82 (1): 3545. doi:10.1115/1.3662552
- [96] The ATLAS Collaboration, Performance of primary vertex reconstruction in proton-proton collisions at $s = \sqrt{7}$ TeV in the ATLAS experiment. ATLAS-CONF-2010-069.
- [97] R. Fruhwirth, W. Waltenberger, P. Vanlaer, *Adaptive vertex fitting*, J. Phys. G34 (2007).
- [98] The ATLAS Collaboration, *Characterization of Interaction-Point Beam Parameters Using the pp Event-Vertex Distribution Reconstructed in the ATLAS Detector at the LHC*, ATL-CONF-2010-027.
- [99] The ATLAS collaboration, *Expected electron performance in the ATLAS experiment*, ATL-PHYS-PUB-2011-006
- [100] The ATLAS Collaboration, *Electron reconstruction and identification efficiency measurements with the ATLAS detector using the 2011 LHC proton-proton collision data*, CERN-PH-EP-2014-040, [arXiv:1404.2240](#)
- [101] The ATLAS Collaboration, G. Aad et al., *Electron performance measurements with the ATLAS detector using the 2010 LHC proton-proton collision data*, Eur.Phys.J. C72 (2012) 1909.
- [102] S. Hassini, et al., *A muon identification and combined reconstruction procedure for the ATLAS detector at the LHC using the (MUONBOY, STACO, MuTag) reconstruction packages*, NIM A572 (2007) 7779.

- [103] The ATLAS Collaboration, G. Aad et al., *Preliminary results on the muon reconstruction efficiency, momentum resolution, and momentum scale in ATLAS 2012 pp collision data*, ATLAS-CONF-2013-088, CERN, 2013,
- [104] M. Cacciari, G. P. Salam, and G. Soyez, *FastJet user manual*, Eur.Phys.J. C72 (2012) 1896.
- [105] W. Lampl et al., *Calorimeter Clustering Algorithms : Description and Performance*, ATL-LARG-PUB-2008-002.
- [106] M. Cacciari, G. P. Salam, and G. Soyez, *The anti-kt jet clustering algorithm*, JHEP 04 (2008) 63.
- [107] E. Abat, J. Abdallah, T. Addy, P. Adragna, et al., *Combined performance studies for electrons at the 2004 ATLAS combined test-beam*, JINST 5 (2010) P11006.
- [108] ATLAS Collaboration, *Jet energy measurement with the ATLAS detector in proton-proton collisions at $\sqrt{s} = 7$ TeV*, Submitted to EPJ (2011) , arXiv:1112.6426
- [109] The ATLAS Collaboration, *Pile-up corrections for jets from proton-proton collisions at ATLAS in 2011*, ATLAS-CONF-2012-064, July, 2012.
- [110] M. Cacciari and G. P. Salam, *Pileup subtraction using jet areas*, Phys.Lett. B659 (2008) 119.
- [111] The ATLAS Collaboration, G. Aad et al., *Jet energy resolution in proton-proton collisions at $\sqrt{s} = 7$ TeV recorded in 2010 with the ATLAS detector*, Eur.Phys.J. C73 (2013) 2306
- [112] The ATLAS collaboration, *Jet energy scale and its systematic uncertainty in proton-proton collisions at $\sqrt{s} = 7$ TeV with ATLAS 2011 data*, ATLAS-CONF-2013-004

- [113] The ATLAS Collaboration, *Data-Quality Requirements and Event Cleaning for Jets and Missing Transverse Energy Reconstruction with the ATLAS Detector in Proton-Proton Collisions at a Center-of-Mass Energy of $\sqrt{s} = 7$ TeV*, ATLAS-CONF-2010-038.
- [114] G. Piacquadio, C. Weiser, *A new inclusive secondary vertex algorithm for b -jet tagging in ATLAS*, JPCS 119 (2008) 032032
- [115] The ATLAS Collaboration, G. Aad et al., *Commissioning of the ATLAS high-performance b -tagging algorithms in the 7 TeV collision data*, ATLAS-CONF-2011-102, CERN, 2011, ATLAS-CONF-2011-102.
- [116] The ATLAS Collaboration, *Measuring the b -tag efficiency in a $t\bar{t}$ sample with 4.7 fb^{-1} of data from the ATLAS detector* ATLAS-CONF-2012-097.
- [117] The ATLAS Collaboration, *Calibration of b -tagging using dileptonic top pair events in a combinatorial likelihood approach with the ATLAS experiment* ATLAS-CONF-2014-004.
- [118] The ATLAS Collaboration, *Reconstruction and Calibration of Missing Transverse Energy and Performance in Z and W events in ATLAS Proton-Proton Collisions at $\sqrt{s}=7$ TeV*, ATLAS-CONF-2011-080.
- [119] ATLAS Collaboration, G. Aad et al., *Performance of missing transverse momentum reconstruction in proton-proton collisions at 7 TeV with ATLAS*, Eur.Phys.J. C72 (2012) 1844.
- [120] The ATLAS Collaboration, *Performance of the Reconstruction and Identification of Hadronic tau Decays in ATLAS with 2011 Data*, ATLAS-CONF-2012-142.
- [121] The ATLAS Collaboration, G. Aad et al., *Performance of the ATLAS trigger system in 2010*, Eur.Phys.J. C72 (2012) 1849.
- [122] The ATLAS Collaboration, G. Aad et al., *Performance of the ATLAS muon trigger in 2011*, ATLAS-CONF-2012-099, CERN, 2012.

- [123] The ATLAS Collaboration, G. Aad et al., *Performance of the ATLAS electron and photon trigger in p-p collisions at $\sqrt{s} = 7$ TeV in 2011*, ATLAS-CONF-2012-048, CERN, 2012.
- [124] M. Dobbs and J.B. Hansen, *The HepMC C++ Monte Carlo Event Record for High Energy Physics*, Computer Physics Communications, ATL-SOFT-2000-001.
- [125] The ATLAS Collaboration, *Evidence for the spin-0 nature of the Higgs boson using ATLAS data*, Phys. Lett. B 726 (2013), pp. 120-144.
- [126] The ATLAS Collaboration, *Measurements of Higgs boson production and couplings in diboson final states with the ATLAS detector at the LHC*, Phys. Lett. B 726 (2013), pp. 88-119.
- [127] The CMS Collaboration, “*Evidence for the direct decay of the 125 GeV Higgs boson to fermions*,” arXiv:1401.6527 [hep-ex].
- [128] The CMS Collaboration, *Higgs boson width from on- vs. off-shell production and decay to Z-boson pairs*, arXiv:1405.3455.
- [129] A. Elagin, P. Murat, A. Pranko, and A. Safonov, *A New Mass Reconstruction Technique for Resonances Decaying to di-tau*, arXiv:1012.4686 [hep-ex]. * Temporary entry *.
- [130] T. A. Collaboration, *Search for neutral MSSM Higgs bosons decaying to $\tau\tau$ pairs in proton-proton collisions at with the ATLAS detector*, Physics Letters B **705** (2011) no. 3, 174 – 192.
- [131] The ATLAS Collaboration, *Data-driven estimation of the background to charged Higgs boson searches using hadronically-decaying tau final states in ATLAS*, ATLAS-CONF-2011-051.
- [132] The ATLAS Collaboration, *Measurement of the $Z \rightarrow \tau\tau$ cross section with the ATLAS detector*, Phys. Rev. D **84** (2011) 112006.

- [133] T. A. Collaboration, *Search for the neutral Higgs bosons of the Minimal Supersymmetric Standard Model in pp collisions at $\sqrt{s} = 7$ TeV with the ATLAS detector*, JHEP , [arXiv:1211.6956](#).
- [134] Atlas statistics forum, *ABCD method in searches*, [link](#)
- [135] The ATLAS Collaboration, *Search for Neutral MSSM Higgs Bosons H to $\tau\tau$ to $l\tau_h$ with the ATLAS Detector in 7 TeV Collisions*, ATL-COM-PHYS-2012-094.
- [136] The ATLAS Collaboration, *Search for neutral Higgs Bosons in the decay mode $H \rightarrow \tau\tau \rightarrow ll + 4\nu$ in proton proton collision at $\sqrt{7}$ TeV with the ATLAS Detector*, ATL-COM-PHYS-2011-758.
- [137] The Atlas Collaboration, *Measurement of the $t\bar{t}$ production cross-section in pp collisions at $\sqrt{s} = 8$ TeV using e-mu events with b-tagged jets* . ATLAS-CONF-2013-097.
- [138] T. Sjostrand, S. Mrenna and P. Skands, *PYTHIA 6.4 physics and manual*, JHEP **05** (2006) 026.
- [139] A. B. et al., *Rivet user manual*, [arXiv:1003.0694](#) [hep-ph].
- [140] The ATLAS and CMS Collaborations, *Procedure for the LHC Higgs boson search combination in summer 2011*, ATL-PHYS-PUB-2011-011, ATL-COM-PHYS-2011-818, CMS-NOTE-2011-005.
- [141] W. Verkerke and D. P. Kirkby, *The RooFit Toolkit for Data Modeling*, eConf C0303241 (2003) MOLT007, [arXiv:physics/0306116](#)
- [142] K. S. Cranmer et al., *The Roostats Project*, PoS ACAT2010 (2010) 57.
- [143] K. Cranmer, G. Lewis, L. Moneta, A. Shibata, and W. Verkerke, *Histfactory: A Tool for Creating Statistical Models for use with RooFit and Roostats*, CERNOPEN2012016 (2012)

- [144] E. G. G. Cowan, K. Cranmer and O. Vitells, *Asymptotic formulae for likelihood-based tests of new physics*, [arXiv:1007.1727 \[hep-ex\]](#).
- [145] A. L. Read. *Presentation of search results: the CLs technique*. J. Phys. G: Nucl. Part. Phys., 28, 2002.
- [146] A. L. Read. *Modified frequentist analysis of search results (the CLs method)*. In Proceedings of the First Workshop on Confidence Limits, CERN, Geneva, Switzerland, 2000.
- [147] LHC Higgs Cross Section Working Group, S. Dittmaier, C. Mariotti, G. Passarino, R. Tanaka (Eds.), et al., *Handbook of LHC Higgs Cross Sections: 1. Inclusive Observables*, [arXiv:1101.0593 \[hep-ph\]](#).
- [148] LHC Higgs Cross Section Working Group, S. Dittmaier, C. Mariotti, G. Passarino, and R. Tanaka (Eds.), *Handbook of LHC Higgs Cross Sections: 2. Differential Distributions*, CERN-2012-002 (CERN, Geneva, 2012) , [arXiv:1201.3084 \[hep-ph\]](#).
- [149] ATLAS collaboration *Performance of the ATLAS Silicon Pattern Recognition Algorithm in Data and Simulation at $\sqrt{s} = 7$ TeV*, ATLAS-CONF-2010-072
- [150] The ATLAS Collaboration, *A measurement of the material in the ATLAS inner detector using secondary hadronic interactions*, [arXiv:1110.6191](#), JINST 7 (2012) P01013
- [151] The ATLAS Collaboration, *Validation of the ATLAS jet energy scale uncertainties using tracks in proton-proton collision $\sqrt{s} = 7$ TeV*, ATLAS-CONF-2011-067
- [152] The ATLAS Collaboration, *Track Reconstruction Efficiency in $\sqrt{s} = 7$ TeV Data for Tracks with $p_T > 100$ MeV*, ATL-PHYS-INT-2010-112
- [153] D. de Florian, G. Ferrera, M. Grazzini and D. Tommasini, *Transverse-momentum resummation: Higgs boson production at the Tevatron and the LHC*, JHEP **1111** (2011) , [arXiv:1109.2109 \[hep-ph\]](#).

- [154] Statistical twiki, NuisanceCheck. <https://twiki.cern.ch/twiki/bin/view/AtlasProtected/Nuisance>

Appendix A

QCD Trigger bias

The single electron trigger (EF_e24vhi_medium1) used in this analysis includes the following isolation cut: $p_T(\text{cone})20/p_T < 0.1$. This means that the kinematical distributions in the anti-isolated ABCD regions will be biased due to a reduced efficiency for high p_T electrons. This unwanted feature may potentially effect the R_{QCD} factor, as the OS/SS ratio may differ due to different p_T spectrum. To check the effect on R_{QCD} the ABCD method has been repeated using the EF_e24vh_medium1 trigger, which doesn't include isolation and hence is prescaled in 2012 8 TeV data. The prescale of a factor around 100 has been taken in consideration using trigger information stored in D3PD. Figure A.1 shows $p_T(\text{cone})$ distribution for the standard and test triggers. The comparable event yields in the region $p_T(\text{cone})20/p_T < 0.1$ show that the prescale normalisation for the test trigger has been correctly accounted for.

Figure A.2 shows the behaviour of R_{QCD} factor as a function of isolation variable for the two triggers under test. As the deviations are within statistical uncertainty, we conclude that the isolation requirement used at trigger level does not influence the OS/SS ratio. Hence no further systematic uncertainty is assigned.

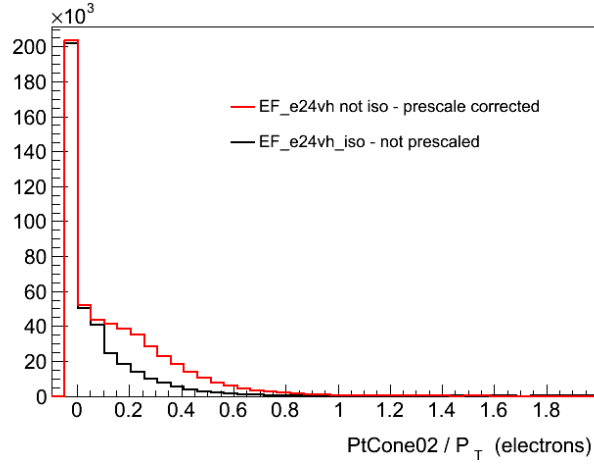


Figure A.1: $p_T(\text{cone}) / p_T$ distribution for the analysis standard trigger and its cor-
 respective without isolation requirement, this second trigger is rescaled according
 to prescales information.

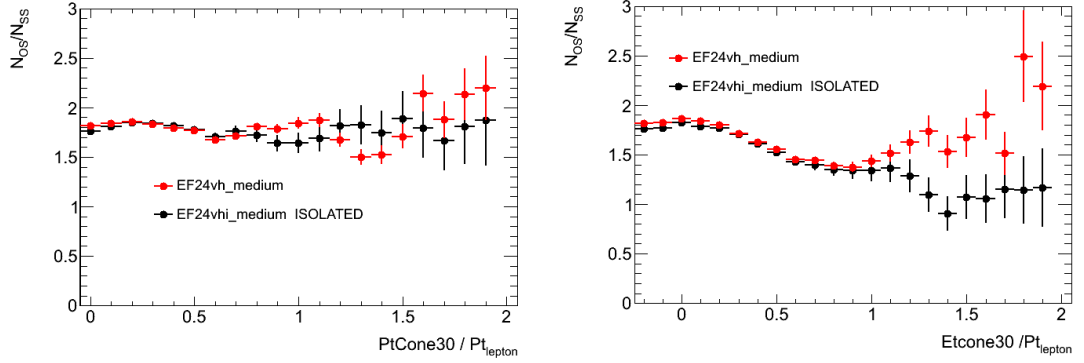


Figure A.2: R_{QCD} as a function of (a) $p_T(\text{cone}) / p_T$ and (b) $E_T(\text{cone}) / PT$ for
 the electron triggers with and without isolation requirement.

Appendix B

QCD Additional Plots

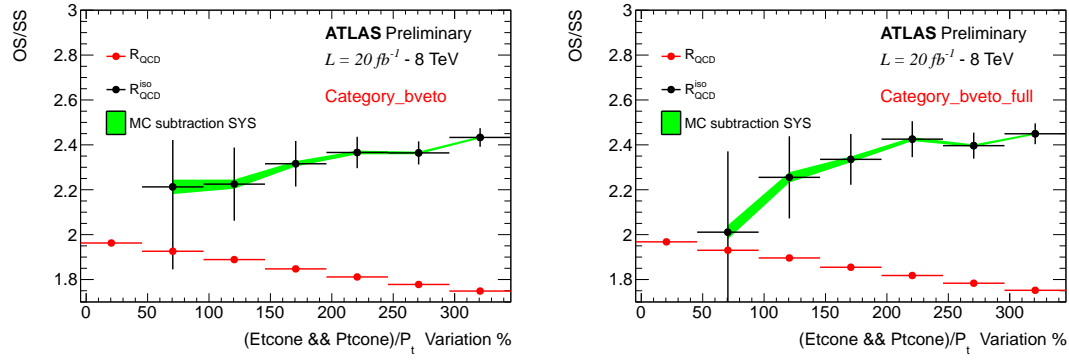


Figure B.1: OS/SS ratio as a function of lepton isolation variable selections (a) after the requirement of zero b-jets and (b) for the full b-veto selection. The isolation selections are varied as a percentage relative to the standard lepton isolation cut values (0 in the plot). The red points show the anti-isolated scale factor R_{QCD} , i.e. the ratio between regions C and D. The black points show the isolated SF, which is defined as the ratio between region \hat{A} and \hat{B} , where the leptons have isolation values larger than the nominal value but smaller than the sliding cut.

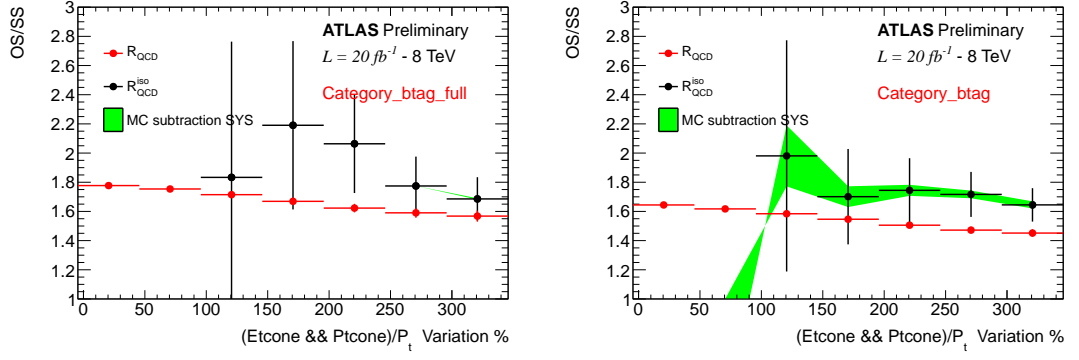


Figure B.2: OS/SS ratio as a function of lepton isolation variable selections (a) after the requirement of one b-jet and (b) for the full b-tag selection. The isolation selections are varied as a percentage relative to the standard lepton isolation cut values (0 in the plot). The red points show the anti-isolated scale factor R_{QCD} , i.e. the ratio between regions C and D. The black points show the isolated SF, which is defined as the ratio between region \hat{A} and \hat{B} , where the leptons have isolation values larger than the nominal value but smaller than the sliding cut.

Appendix C

Limits cross checks and additional plots

C.1 The ABCD Method

The actual implementation in the limit framework of the ABCD method follows that suggested in [134]. The control data samples B,C and D are considered as additional channels to be statistically combined to two the signal event category. Three free parameters are fitted in B,C and D channels which are: the number of multi-jet events in the data sample B, N_B^{QCD} , the factor R_{QCD} and the factor that extrapolates from isolated to anti-isolated data control samples R_{BD} . Neglecting signal contributions, the following equations can be written for the event yield of the B,C and D control data samples:

$$N_B = N_B^{BKG} + N_B^{QCD}$$

$$N_C = N_C^{BKG} + N_B^{QCD} \times R_{QCD} \times R_{BD}$$

$$N_D = N_D^{BKG} + N_B^{QCD} \times R_{BD}$$

where N^{BKG} represent the prediction of non-QCD background in the relative data samples. The estimate of multi-jet event yield in the signal sample will be then $N_B^{QCD} \times R_{QCD}$. This method is particularly powerful because in the best fit of

R_{QCD} the statistical and systematics uncertainty for non-QCD backgrounds and data are considered.

C.2 Additional Limit Checks

During the limit derivation, the systematic uncertainties (translated in term of nuisance parameter) are fitted to the data, several checks are have been performed to ensure the quality of our statistical model. If some of the nuisance parameters are significantly different from their nominal value (ie before fit), it can be symptomatic of an important mis-modelling and must be carefully scrutinised. Also the correlation between the nuisance parameter and the signal strength (which reflects the degeneracy of the fit) is an important element to keep under control, in fact it reflects how well the data can constraint the nuisance parameters. Finally, to have a feeling of the behaviour of the likelihood at its minimum one can check the negative log likelihood profile in each nuisance parameter direction. We performed all this checks using the package NuisanceCheck-00-00-05 described in [154].

The signal and background model with the signal normalisation free (unconditional fit) is fitted to the data, in the following example plots the signal is assumed for the mass point $m_A = 120$ GeV, $\tan\beta = 20$, The difference between the post fit and pre-fit value of the nuisance parameter along with their errors is shown in figure C.1-C.3, respectively for the b-veto, b-tag channel and the combination between them. Figure C.4-C.6 shows the correlation matrix between the nuisance parameters respectively for the veto category, tag category and the combination between the two channels. Figure C.7-C.9 shows the behaviour of the likelihood at its minimum for each of the nuisance parameters (while a nuisance parameter is investigated the other are kept constant) for the combination between the channels.

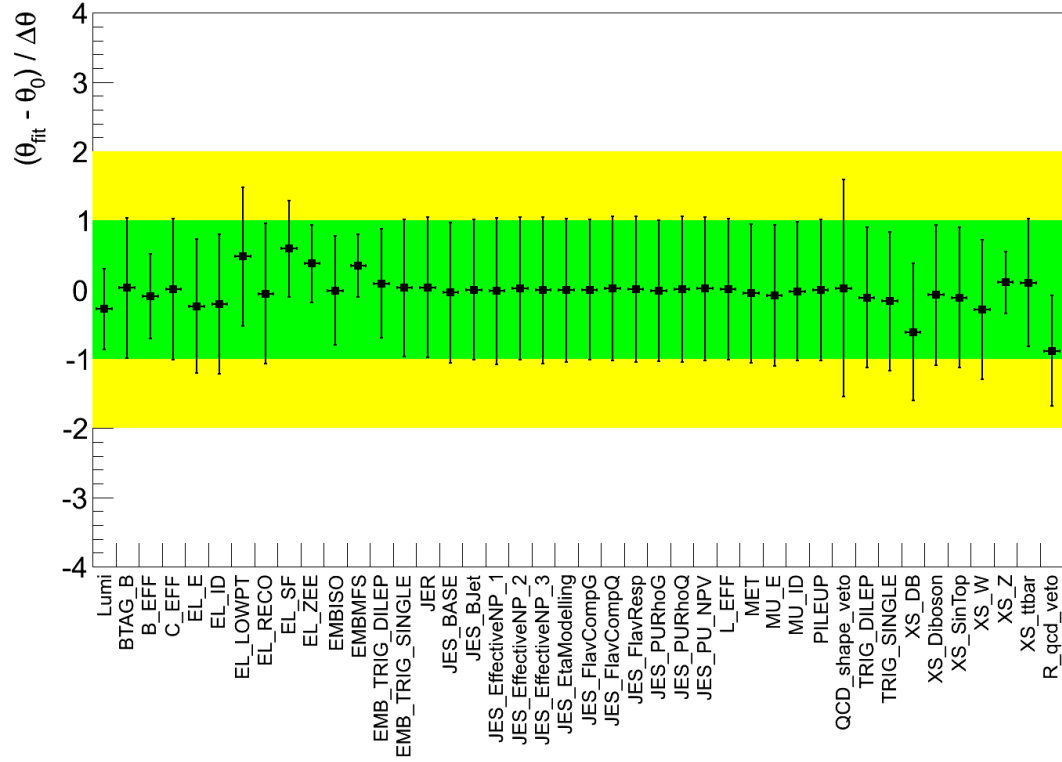


Figure C.1: Pulls for nuisance parameter considered in the fit, $m_A = 120$ GeV, $\tan\beta = 20$, for the veto channel.

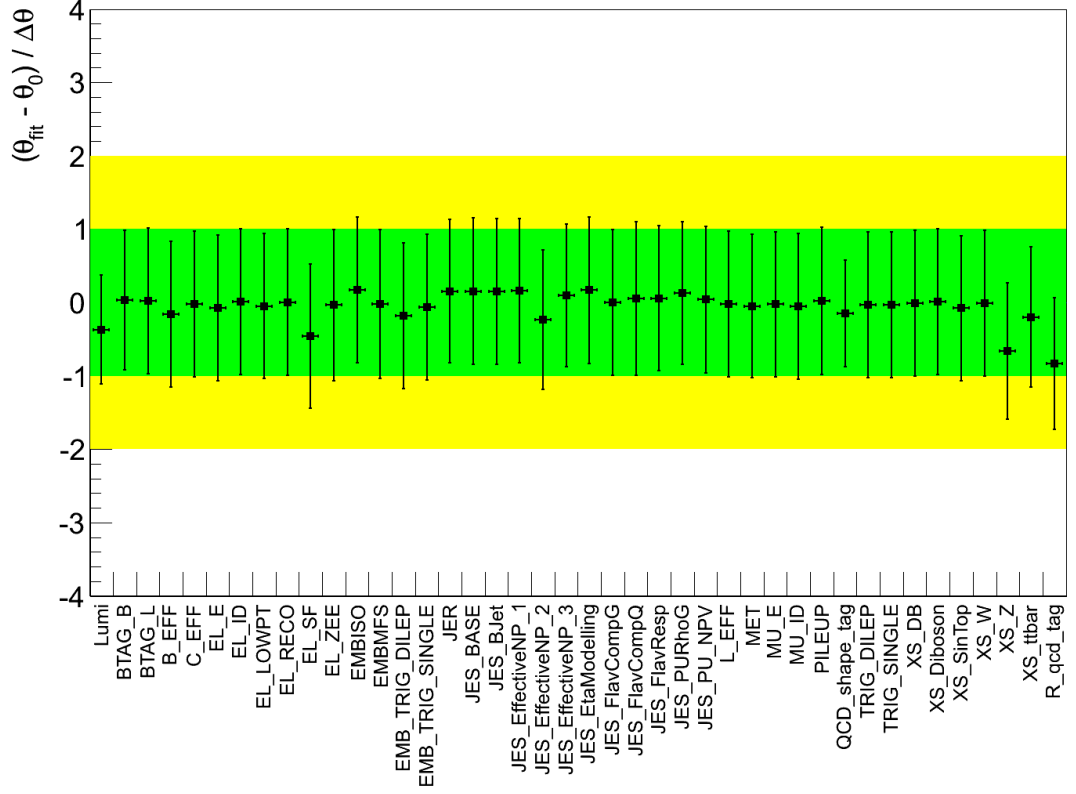


Figure C.2: Pulls for nuisance parameter considered in the fit, $m_A = 120$ GeV, $\tan\beta = 20$, for the tag channel.

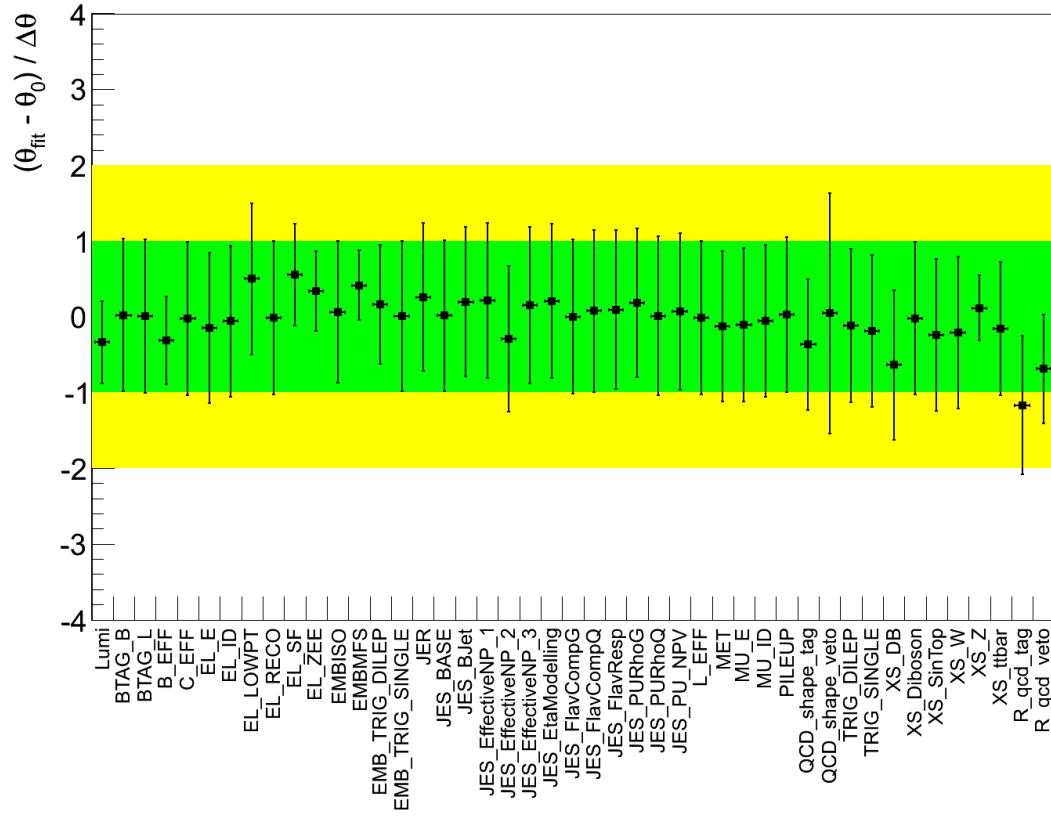


Figure C.3: Pulls for nuisance parameter considered in the fit, $m_A = 120$ GeV, $\tan\beta = 20$, combination between the two channel.

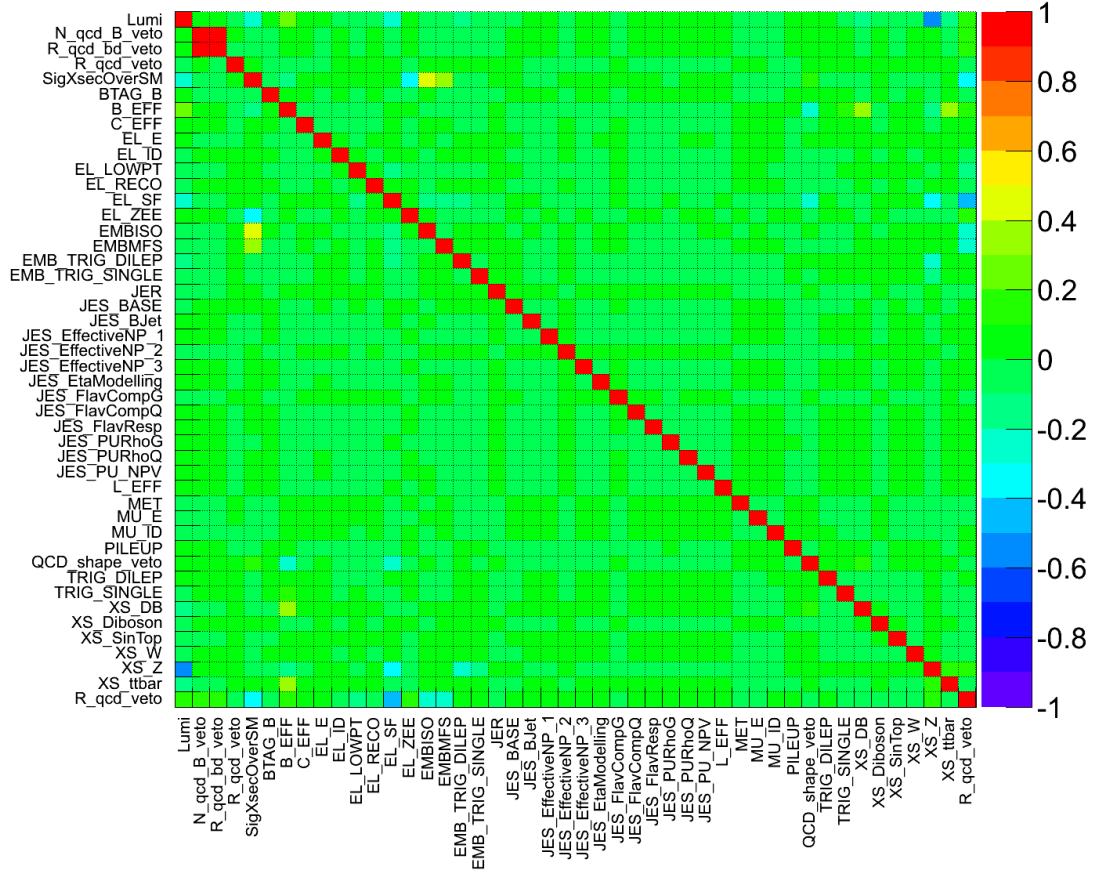


Figure C.4: Correlation matrix for nuisance parameters considered in the fit. The point $m_A = 120$ GeV and $\tan\beta = 20$ is considered for the tag channel.

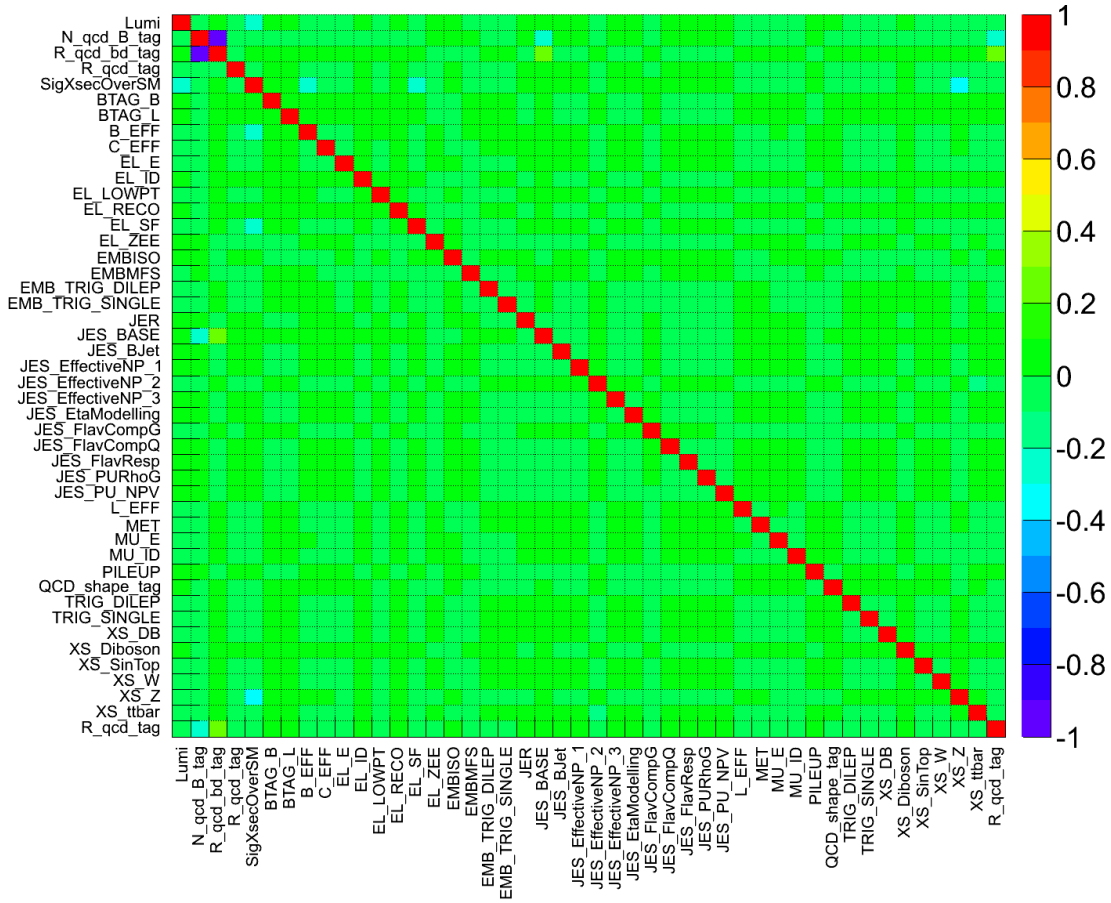


Figure C.5: Correlation matrix for nuisance parameters considered in the fit. The point $m_A = 120$ GeV and $\tan\beta = 20$ is considered for the tag channel.

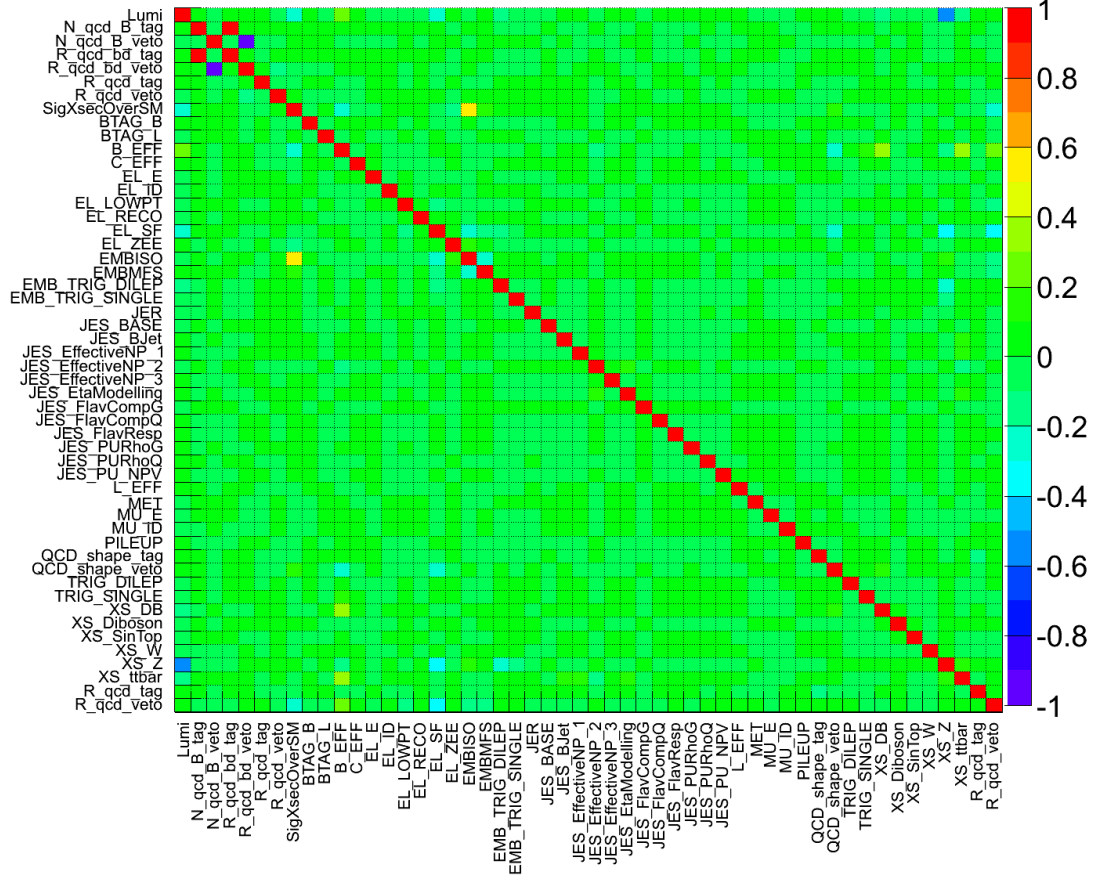


Figure C.6: Correlation matrix for nuisance parameters considered in the fit. The point $m_A = 120$ GeV and $\tan\beta = 20$ is considered for the combination of the b-tag and b-veto channels.

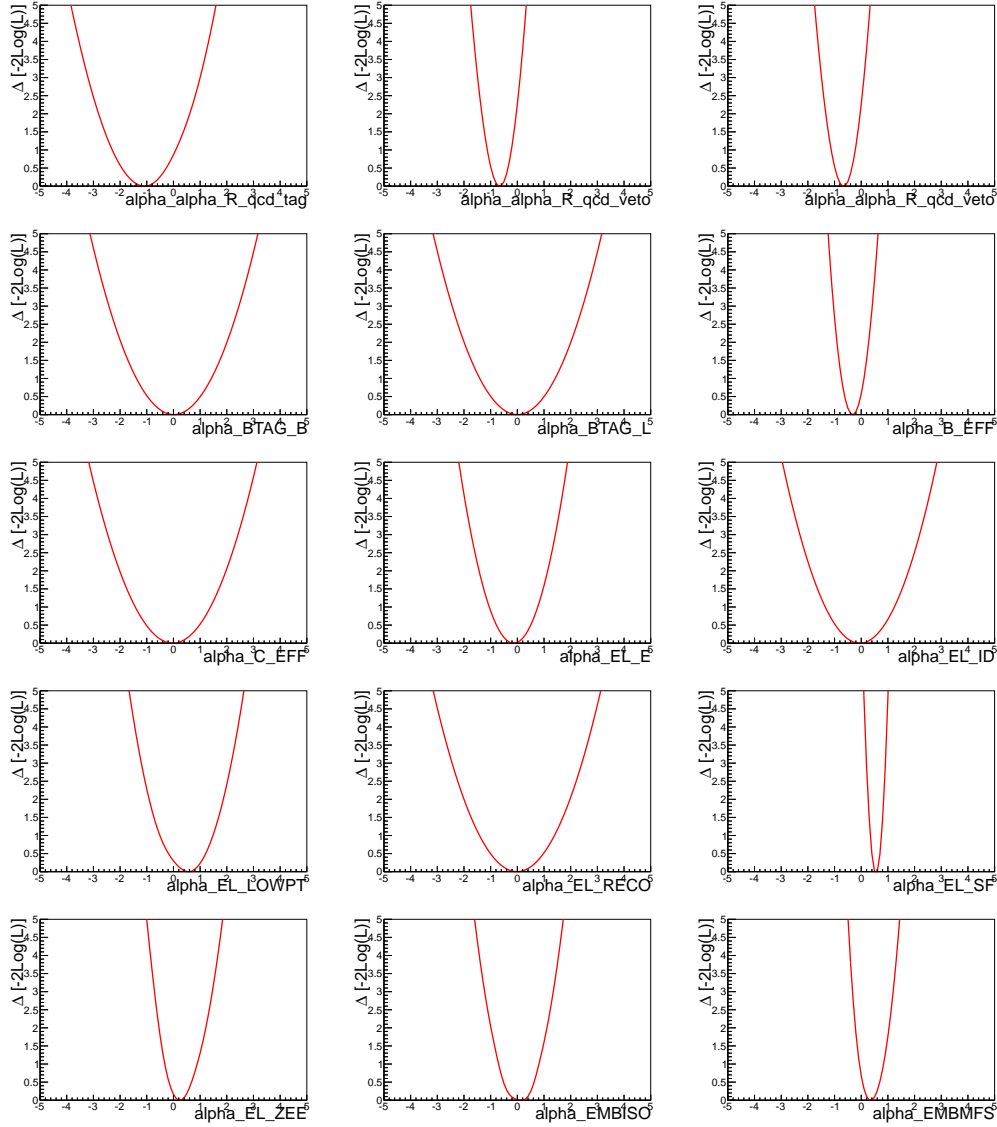


Figure C.7: Likelihood scans for nuisance parameter considered in the fit, $m_A = 120$ GeV, $\tan\beta = 20$, combination between the two channel.

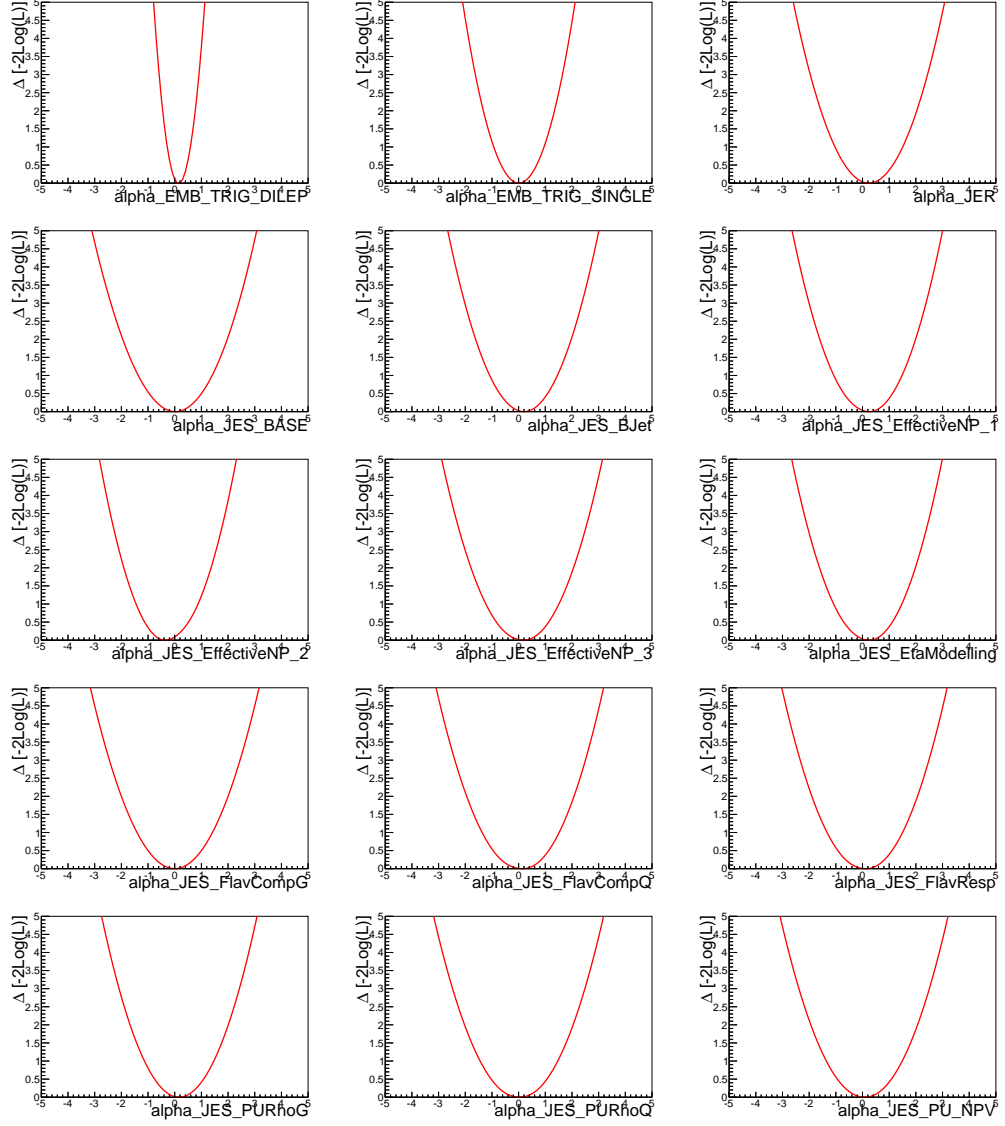


Figure C.8: Likelihood scans for nuisance parameter considered in the fit, $m_A = 120$ GeV, $\tan\beta = 20$, combination between the two channel.

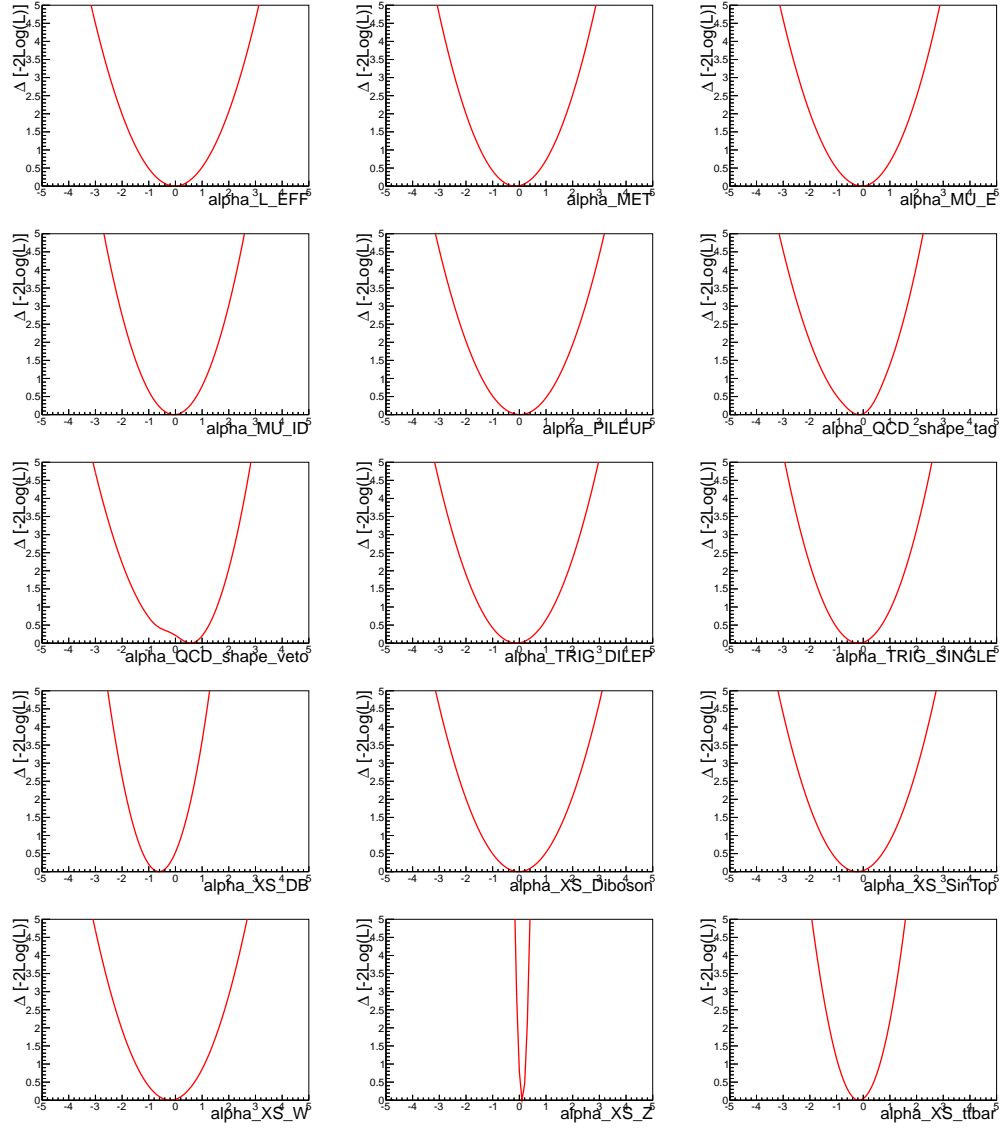


Figure C.9: Likelihood scans for nuisance parameter considered in the fit, $m_A = 120$ GeV, $\tan\beta = 20$, combination between the two channel.

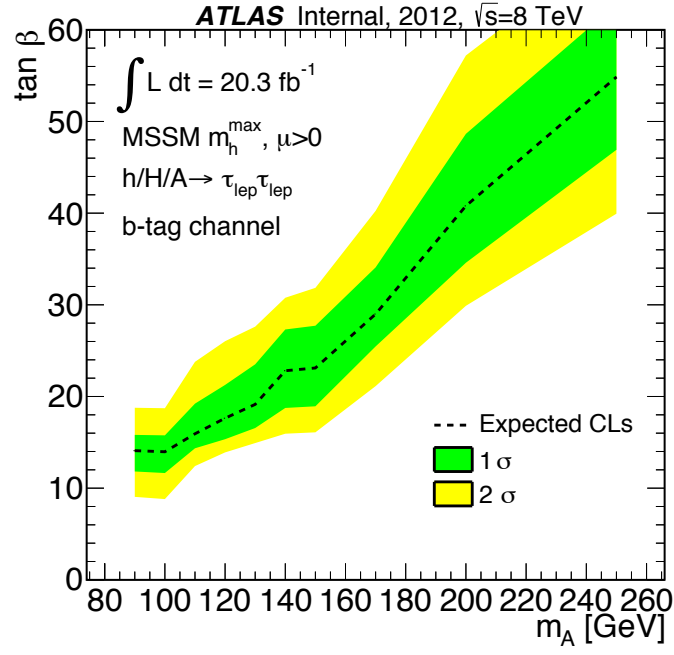


Figure C.10: Expected exclusion limits, using the b-tag channel, for MSSM Higgs boson production in the MSSM m_A vs $\tan \beta$ parameter space.

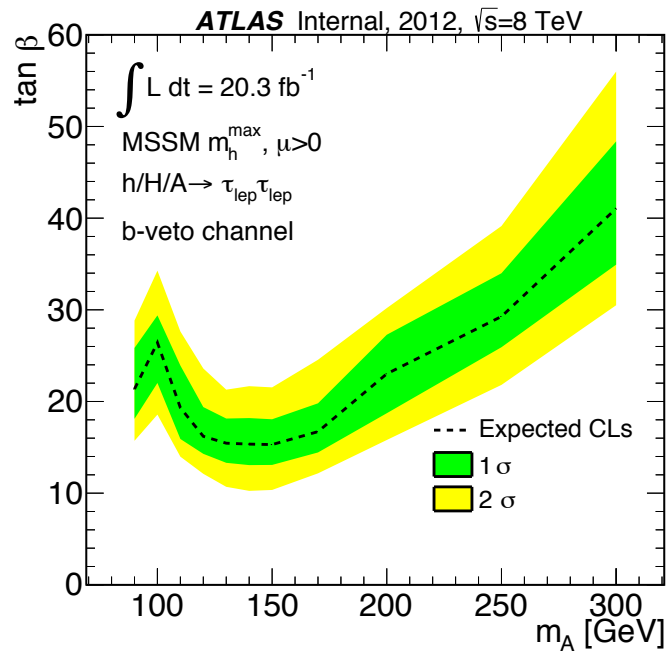


Figure C.11: Expected exclusion limits, using the b-veto channel, for MSSM Higgs boson production in the MSSM m_A vs $\tan \beta$ parameter space.

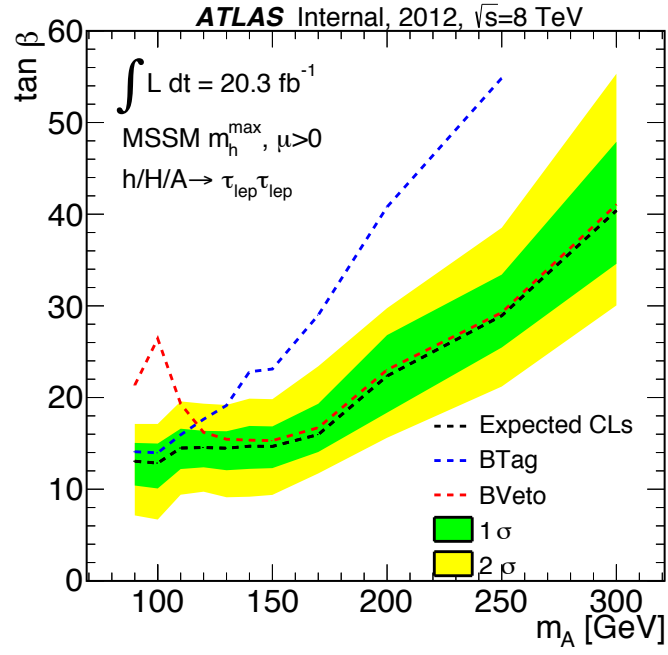
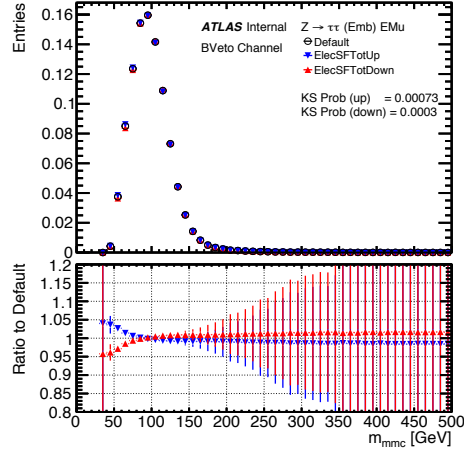
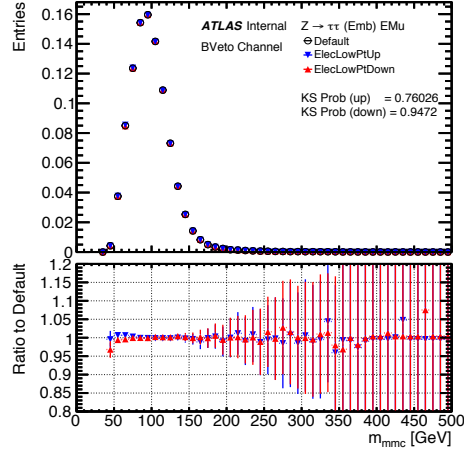


Figure C.12: Expected exclusion limits for MSSM Higgs boson production in the MSSM m_A vs $\tan \beta$ parameter space. Limits are compared for the b-tag and b-veto channel with the combined limit from both channels.

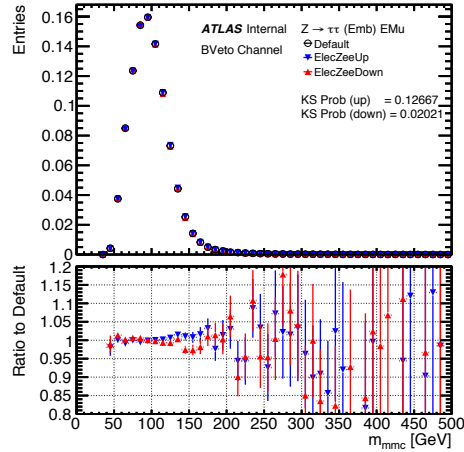
C.3 Shape Systematics



(a)



(b)



(c)

Figure C.13: Effect on the $m_{\tau\tau}^{MMC}$ distribution of the embedding sample due to the (a) the electron reconstruction and identification systematics, (b) the electron low p_T energy scale systematic and (c) the electron Zee energy scale systematic. The plots are made after the full b-veto category selection.